3-2005

Numerical Analysis and Optimization of the Ultra Compact Combustors

Roger T. Greenwood

NUMERICAL ANALYSIS AND OPTIMIZATION OF THE ULTRA COMPACT COMBUSTOR

THESIS

Roger T. Greenwood, Captain, USAF

AFIT/GAE/ENY/05-M10

DEPARTMENT OF THE AIR FORCE
AIR UNIVERSITY

AIR FORCE INSTITUTE OF TECHNOLOGY

Wright-Patterson Air Force Base, Ohio

The views expressed in this thesis are those of the author and do not reflect the official policy or position of the United States Air Force, Department of Defense, or the United States Government

AFIT/GAE/ENY/05-M10

NUMERICAL ANALYSIS AND OPTIMIZATION OF THE ULTRA COMPACT COMBUSTOR

THESIS

Presented to the Faculty

Department of Aeronautics and Astronautics

Graduate School of Engineering and Management

Air Force Institute of Technology

Air University

Air Education and Training Command

In Partial Fulfillment of the Requirements for the

Degree of Master of Science in Aeronautical Engineering

Roger T. Greenwood, B.S.

Captain, USAF

March 2005

AFIT/GAE/ENY/05-M10

NUMERICAL ANALYSIS AND OPTIMIZATION OF THE ULTRA COMPACT COMBUSTOR

Roger T. Greenwood, B.S.
Captain, USAF

Approved:

/signed/	21 Mar 2005
Dr. Ralph Anthenien (Chairman)	date
/signed/	21 Mar 2005
Dr. Mark Reeder (Member)	date
/signed/	21 Mar 2005
Maj Richard McMullan (Member)	date

Abstract

In an effort to increase thrust per weight ratio and decrease pollutant emissions of aero-turbine jet engines, a circumferentially burning Ultra Compact Combustor (UCC) with a Cavity-in-a-Cavity design has been developed. A numerical analysis of this design has been conducted and compared with experimental results to validate the numerical model. This numerical model was then used to optimize the design of the UCC cycle/components.

A commercial Computational Fluid Dynamics (CFD) package with a k-ϵ turbulence model was used throughout the process to model the flow and combustion process through the combustor. The CFD results compared favorably with the experimental results over a wide range of inlet pressures and temperatures, as well as static pressure drops and equivalence ratios, to serve as a validation of the CFD model. Inlet mach numbers for the range of test conditions were between 0.11 and 0.25.

The CFD model has been validated through a wide range of conditions and four alternative physical configurations of the UCC have been modeled. The first alternative configuration consisted of an increased outflow area 26 percent larger than the original design. The second variation tested the impact of maintaining mass flow rate into the cavity while significantly decreasing the velocity. The third configuration modeled the effect of a decreased cavity length of 80% the original length. The final configuration maintained the decreased cavity length of the last configuration and added curvature to the vane. These various configurations were compared as an initial step leading to an optimization of the design, using emissions, combustor efficiencies, temperature and velocity profiles, and pressure drop values as comparison parameters.

Results of this analysis are a key step in producing an optimized UCC design. They indicate that increasing the outflow area will increase the pressure drop over the combustor and decrease the combustor efficiency by nearly 4% at lower pressures. However, this increased outflow configuration shows some promise at the higher pres-

sures and further investigation should be conducted. It was also determined that a significant decrease (250%) in the cavity circumferential velocity effectively decreased the fuel-air mixing in the cavity resulting in decreased combustion efficiencies of up to nearly 3% less than the original configuration.

For the five operating conditions tested, the decreased cavity length configuration decreased pressure drop values by about 4 to 10% with only minimal increases in pollutant emissions. Also, for each operating condition, the combustor efficiency of the decreased cavity length was within 1% the efficiency of the original configuration. The addition of a curved vane to the decreased cavity length configuration further decreased the pressure drop while maintaining a comparable combustor efficiency. It is believed that further design optimizations on this decreased cavity length configuration will produce significant weight savings and decrease pressure losses with minimal combustion efficiency impact.

Acknowledgements

This work was accomplished with the help and support of many individuals, both directly and indirectly, and I would like to express my appreciation to them. This includes both the students and faculty for their association and teaching during this time here at AFIT.

I would also like to thank Dr. Julian Tishkoff from the Air Force Office of Scientific Research/NA and Dr. Robert Hancock from Air Force Research Laboratory/PRTS for their financial support in this endeavor. My appreciation also goes to Dr. Joe Zelina, also from AFRL/PRTS, who has been a tremendous assistance as problems and questions have arisen.

My advisor, Dr. Ralph Anthenien who has answered my questions, given me guidance and encouragement, pinpointed problems, and has been a tremendous help throughout this process, always reminding me that if it were easy, someone would already have done it.

My family has helped me remain sane throughout this experience and I would like to thank them for helping me always remember that which is most important. I would like to thank my lovely wife for her love, patience, and support throughout this experience. I would also like to thank my daughters for their goodness and for giving me a reason to smile each and every day.

And finally, I would like to thank the Almighty for His many blessings which have allowed me to accomplish this work and, for the most part, enjoy the journey.

Table of Contents

Page

Abstract iv

Acknowledgements vi

List of Figures x

List of Tables xiv

List of Abbreviations xv

List of Symbols xvi

I. Introduction and Overview 1-1
- 1.1 Historical Perspective 1-1
- 1.2 Conceptual Design 1-2
- 1.3 Motivation 1-3
- 1.4 Evalution Criteria 1-6
- 1.5 Research Outline 1-8

II. Background and Theory 2-1
- 2.1 Literature Review 2-1
  - 2.1.1 Trapped Vortex 2-1
  - 2.1.2 Centrifugal Force Combustion 2-2
- 2.2 Emissions 2-3
- 2.3 Temperature Pattern and Profile 2-5
- 2.4 Inter-Turbine Burner 2-6
- 2.5 Heat Transfer 2-7
- 2.6 Computational Fluid Dynamics 2-9
  - 2.6.1 Relaxation Parameters 2-9
  - 2.6.2 Turbulence Modeling 2-9
  - 2.6.3 Species Modeling 2-10
  - 2.6.4 NO_x Modeling 2-11

III. Experimental Configurations 3-1
- 3.1 Experimental Procedure 3-1
  - 3.1.1 Experiments 3-1
- 3.2 Numerical Procedure 3-2
  - 3.2.1 Grid Construction 3-3
  - 3.2.2 Species Modeling 3-3

Page

3.2.3 Operating Conditions 3-5
3.2.4 Pollutant Modeling 3-5
3.2.5 Turbulence Modeling 3-6
3.2.6 Fuel Injection 3-6
3.2.7 Boundary Conditions 3-7

IV. Results and Discussion 4-1
4.1 Validation of CFD Model 4-1
4.2 Impact of Increased Outflow Area 4-5
4.2.1 Efficiency and Emissions Impact 4-5
4.2.2 Cavity Velocity Profiles 4-7
4.2.3 Pressure Loss Comparison 4-8
4.2.4 Temperature Pattern and Profile 4-10
4.3 Impact of Decreased Cavity Jet Velocity 4-11
4.3.1 Efficiency and Emissions Impact 4-12
4.3.2 Cavity Velocity Profiles 4-12
4.3.3 Pressure Loss Comparison 4-13
4.3.4 Temperature Pattern and Profile 4-14
4.4 Impact of Decreased Cavity Length 4-15
4.4.1 Efficiency and Emissions Impact 4-16
4.4.2 Cavity Velocity Profiles 4-16
4.4.3 Pressure Loss Comparison 4-17
4.4.4 Temperature Pattern and Profile 4-18
4.5 Impact of Vane Curvature 4-20
4.5.1 Efficiency and Emissions Impact 4-20
4.5.2 Cavity Velocity Profiles 4-22
4.5.3 Pressure Loss Comparison 4-22
4.5.4 Temperature Pattern and Profile 4-23
4.6 Design Impact Summary 4-24
4.7 Fuel Droplet Size Comparison 4-25
4.8 Cavity in a Cavity 4-26
4.9 Total Pressure Drop Comparison 4-27
4.10 Overall Combustor Efficiency and Emissions 4-29

V. Conclusion 5-1
5.1 Future Work 5-4

Appendix A
Velocity Contours of Various UCC Configurations 0-6

Page

Appendix B
Velocity Vectors for Experimental Configuration 0-8

Appendix C
Velocity Vectors for Increased Outlet Area Configuration 0-10

Appendix D
Velocity Vectors for Decreased Cavity Velocity Configuration . . . 0-12

Appendix E
Velocity Vectors for Decreased Cavity Length Configuration . . . 0-14

Appendix F
Velocity Vectors for Decreased Cavity Length with Curved Vane . 0-16

Bibliography 18

Vita 20

List of Figures

Figure		Page
1.1.	Vortex Combustion Concept.	1-2
1.2.	Ultra Compact Combustor.	1-4
3.1.	Ultra Compact Combustor Numerical Mesh.	3-2
4.1.	Run 1 Temperature Contours at Outlet of Experimental Configuration (Geometry 1)	4-3
4.2.	Run 1 Cutaway Temperature Contours of Experimental Configuration (Geometry 1)	4-3
4.3.	Cavity Velocity Vectors of Baseline Configuration (Geometry 1) on Periodic Boundary (Run 1)	4-4
4.4.	Run 1 Outlet Velocity Contours of Increased Outflow Area (Geometry 2)	4-6
4.5.	Cavity Velocity Vectors of Increased Outflow Area (Geometry 2) on Periodic Boundary (Run 1) *Note the increased outer diameter of this configuration as the flow exits the cavity.	4-7
4.6.	Cavity Velocity Vectors of Increased Outflow Area (Geometry 2) through Cavity Area on Fuel Injector Plane (Run 1)	4-8
4.7.	Run 1 Cross-Section Velocity Vectors of Cavity Area for Increased Outflow Area Configuration (Geometry 2)	4-9
4.8.	Run 1 Temperature Contours at Outlet of Increased Outflow Area (Geometry 2)	4-10
4.9.	Run 1 Cutaway Temperature Contours of Increased Outflow Area (Geometry 2)	4-11
4.10.	Cavity Velocity Vectors (Colored by Temperature Contours) of Decreased Cavity Jet Velocity (Geometry 3) on Periodic Boundary (Run 1)	4-13
4.11.	Run 1 Temperature Contours at Outlet of Decreased Cavity Jet Velocity (Geometry 3)	4-14

Figure Page

4.12. Run 1 Cutaway Temperature Contours of Decreased Cavity Jet Velocity (Geometry 3) 4-15

4.13. Cavity Velocity Vectors of Decreased Cavity Length (Geometry 4) on Periodic Boundary (Run 1) 4-17

4.14. Run 1 Temperature Contours at Outlet of Decreased Cavity Length (Geometry 4) 4-19

4.15. Run 1 Cutaway Temperature Contours of Decreased Cavity Length (Geometry 4) 4-19

4.16. Run 1 Cutaway Temperature Contours of Decreased Cavity Length with Curved Vane (Geometry 5) 4-21

4.17. Cavity Velocity Vectors of Decreased Cavity Length with Curved Vane (Geometry 5) on Periodic Boundary 4-22

4.18. Run 1 Temperature Contours at Outlet of Decreased Cavity Length with Curved Vane (Geometry 5) 4-23

4.19. Configuration Trends as compared with the Baseline Configuration 4-24

4.20. Cavity in a Cavity Velocity Contours 4-26

4.21. Cavity in a Cavity Velocity Contours (in plane with injector) . 4-27

4.22. Total Pressure Drop vs Mass Flow Rate for all Numerical UCC Geometries. 4-28

4.23. NO_x vs Mass Air Flow. 4-29

4.24. CO vs Mass Air Flow. 4-30

4.25. Unburned Hydrocarbons vs Mass Air Flow 4-31

4.26. Emissions Index of Unburned Hydrocarbons vs Mass Air Flow. 4-31

0.1. Run 1 Cutaway Velocity Contours of Experimental Configuration (Geometry 1) 0-6

0.2. Run 1 Cutaway Velocity Contours of Increased Outflow Area (Geometry 2) 0-6

0.3. Run 1 Cutaway Velocity Contours of Decreased Cavity Jet Velocity (Geometry 3) 0-6

Figure Page

0.4. Run 1 Cutaway Velocity Contours of Decreased Cavity Length (Geometry 4) 0-7

0.5. Run 1 Outlet Velocity Contours of Decreased Cavity Length (Geometry 4) 0-7

0.6. Run 1 Outlet Velocity Contours of Decreased Cavity Length with Curved Vane (Geometry 5) 0-7

0.7. Cavity Velocity Vectors of Experimental Configuration (Geometry 1) on Periodic Boundary (Run 2) 0-8

0.8. Cavity Velocity Vectors of Experimental Configuration (Geometry 1) on Periodic Boundary (Run 3) 0-8

0.9. Cavity Velocity Vectors of Experimental Configuration (Geometry 1) on Periodic Boundary (Run 4) 0-9

0.10. Cavity Velocity Vectors of Experimental Configuration (Geometry 1) on Periodic Boundary (Run 5) 0-9

0.11. Cavity Velocity Vectors of Increased Outflow Area Configuration (Geometry 2) on Periodic Boundary (Run 2) 0-10

0.12. Cavity Velocity Vectors of Increased Outflow Area Configuration (Geometry 2) on Periodic Boundary (Run 3) 0-10

0.13. Cavity Velocity Vectors of Increased Outflow Area Configuration (Geometry 2) on Periodic Boundary (Run 4) 0-11

0.14. Cavity Velocity Vectors of Increased Outflow Area Configuration (Geometry 2) on Periodic Boundary (Run 5) 0-11

0.15. Cavity Velocity Vectors of Decreased Cavity Velocity Configuration (Geometry 3) on Periodic Boundary (Run 2) 0-12

0.16. Cavity Velocity Vectors of Decreased Cavity Velocity Configuration (Geometry 3) on Periodic Boundary (Run 3) 0-12

0.17. Cavity Velocity Vectors of Decreased Cavity Velocity Configuration (Geometry 3) on Periodic Boundary (Run 4) 0-13

0.18. Cavity Velocity Vectors of Decreased Cavity Velocity Configuration (Geometry 3) on Periodic Boundary (Run 5) 0-13

0.19. Cavity Velocity Vectors of Decreased Cavity Length Configuration (Geometry 4) on Periodic Boundary (Run 2) 0-14

Figure Page

0.20. Cavity Velocity Vectors of Decreased Cavity Length Configuration (Geometry 4) on Periodic Boundary (Run 3) 0-14

0.21. Cavity Velocity Vectors of Decreased Cavity Length Configuration (Geometry 4) on Periodic Boundary (Run 4) 0-15

0.22. Cavity Velocity Vectors of Decreased Cavity Length Configuration (Geometry 4) on Periodic Boundary (Run 5) 0-15

0.23. Cavity Velocity Vectors of Decreased Cavity Length with Curved Vane (Geometry 5) on Periodic Boundary (Run 2) 0-16

0.24. Cavity Velocity Vectors of Decreased Cavity Length with Curved Vane (Geometry 5) on Periodic Boundary (Run 3) 0-16

0.25. Cavity Velocity Vectors of Decreased Cavity Length with Curved Vane (Geometry 5) on Periodic Boundary (Run 4) 0-17

0.26. Cavity Velocity Vectors of Decreased Cavity Length with Curved Vane (Geometry 5) on Periodic Boundary (Run 5) 0-17

List of Tables

Table		Page
2.1.	Values used in Wall Heat Transfer Calculations	2-8
3.1.	Experimental Run Conditions	3-1
3.2.	Numerical Grid Geometries (*Geometry 1=Baseline Configuration)	3-4
4.1.	Comparison of Experimental vs Numerical Results	4-1
4.2.	Baseline(Geometry 1) vs Increased Outflow Area Configuration(Geometry 2) Emission and Efficiency Comparison	4-5
4.3.	Baseline(Geometry 1) vs Increased Outflow Area Configuration(Geometry 2) Pressure Loss and Pattern Factor Comparison	4-9
4.4.	Baseline(Geometry 1) vs Decreased Cavity Jet Velocity Configuration(Geometry 3) Emission and Efficiency Comparison	4-12
4.5.	Baseline(Geometry 1) vs Decreased Cavity Jet Velocity Configuration(Geometry 3) Pressure Loss and Pattern Factor Comparison	4-14
4.6.	Baseline(Geometry 1) vs Decreased Cavity Length Configuration(Geometry 4) Emission and Efficiency Comparison	4-17
4.7.	Baseline(Geometry 1) vs Decreased Cavity Length Configuration(Geometry 4) Pressure Loss and Pattern Factor Comparison	4-18
4.8.	Decreased Cavity Length Configuration(Geometry 4) vs Decreased Cavity Length with Curved Vane Configuration(Geometry 5) Emission and Efficiency Comparison	4-21
4.9.	Decreased Cavity Length Configuration(Geometry 4) vs Decreased Cavity Length with Curved Vane Configuration(Geometry 5) Pressure Loss and Pattern Factor Comparison	4-23
4.10.	Mean Droplet Injection Diameters Test Conditions	4-25
4.11.	Results of Increased Mean Droplet Injection Diameters	4-26

List of Abbreviations

Abbreviation		Page
UCC	Ultra Compact Combustor	iv
CFD	Computational Fluid Dynamics	iv
TV	Trapped Vortex	1-2
TVC	Trapped Vortex Combustor	1-3
CIAC	Cavity in a Cavity	1-3
MTBM	Mean Time Between Maintainance	1-4
TSFC	Thrust Specific Fuel Consumption (1/hr)	1-4
ICAO	International Civil Aviation Organization	1-4
RQL	Rich Quench Lean Burn	1-5
ITB	Inter-Turbine Burner	1-5
ppm	parts per million	1-6
LBO	Lean Blow Out	2-1
CFD	Computational Fluid Dynamics	2-9
SOR	Successive overrelaxation	2-9
DNS	Direct Numerical Simulation	2-9
RANS	Reynolds Averaged Navier Stokes	2-10
LES	Large Eddy Simulation	2-10
FN	Flow Number	3-1
SMD	Sauder Mean Diameter (microns)	3-1
CAD	Computer Aided Design	3-3
IGES	International Graphics Exchange Specification	3-3
PDF	Probability Density Function	3-4
UCC	Ultra Compact Combustor	1

List of Symbols

Symbol		Page
NO_x	Oxides of Nitrogen	1-4
CO	Carbon Monoxide	1-4
HC	Hydrocarbons	1-5
η_b	Combustion Efficiency (%)	1-6
H_C	Heat of Combustion ($\frac{kJ}{kg}$)	1-6
$EI_{pollutant}$	Emissions Index ($\frac{g}{kg}$)	1-6
CO_2	Carbon Dioxide	1-6
H_2O	Water	1-6
O_2	Oxygen	1-6
N_2	Nitrogen	1-6
P_3	Combustor Inlet Pressure (Pa)	1-7
P_4	Combustor Outlet Pressure (Pa)	1-7
T_{max}	Maximum Outlet Temperature (K)	2-5
$T_{4(avg)}$	Average Outlet Temperature (K)	2-5
T_3	Inlet Temperature (K)	2-5
T_{mr}	Maximum Circumferential Mean Temperature (K)	2-5
η_{th}	Thermal Efficiency	2-6
τ_c	Compressor Ratio	2-6
τ_r	Temperature Ratio due to Flight Mach Number	2-6
M_0	Mach Number	2-6
T_{t3}	Total Temperature at Combustor Inlet (K)	2-6
T_{t2}	Total Temperature at the Compressor Inlet (K)	2-6
γ	Ratio of Specific Heats	2-6
ϵ	Emissivity	2-7
$\bar{h}$	Convection Heat Transfer Coefficient ($\frac{W}{m^2K}$)	2-8

Symbol		Page
k	Thermal Conductivity ($\frac{W}{mK}$)	2-8
D	Diameter (m)	2-8
$N\bar{u}_D$	Nusselt number (1)	2-8
Pr	Prandtl Number (1)	2-8
Ra	Rayleigh Number (1)	2-8
β	Volumetric Thermal Expansion Coefficient (1/K)	2-8
ν	Kinematic Viscosity ($\frac{m^2}{s}$)	2-8
α	Thermal Diffusivity ($\frac{m^2}{s}$)	2-8
T_s	Surface Temperature (T)	2-8
T_∞	Far Field Temperature (K)	2-8
g	Acceleration of Gravity ($\frac{m}{s^2}$)	2-8
ω	relaxation parameter	2-9
T	Temperature (K)	3-1
P	Pressure (Pa)	3-1
$\dot{m}_{main}$	Main Air Mass Flow Rate ($\frac{lb}{min}$)	3-1
$\dot{m}_{cavity}$	Cavity Air Mass Flow Rate ($\frac{lb}{min}$)	3-1
Φ	Equivalence Ratio	3-1
A_3	Combustor Inlet Area (in^2)	3-3
A_4	Combustor Outlet Area (in^2)	3-3
D_{jets}	Diameter of Cavity Air Jets (in)	3-3
$C_{12}H_{23}$	Kerosene	3-4
H_2	Hydrogen	3-4
OH	Hydroxide	3-4
C(S)	Carbon	3-4
MM	Molecular Mass ($\frac{g}{mol}$)	3-4
R	Universal Gas Constant ($\frac{J}{molK}$)	3-5
D_{mean}	Droplet Mean Diameter	4-25

NUMERICAL ANALYSIS AND OPTIMIZATION OF THE ULTRA COMPACT COMBUSTOR

I. Introduction and Overview

1.1 Historical Perspective

Since the beginning of powered flights, propulsion research has been directed to the production of lighter, more powerful propulsion systems. The first flight by the Wright Brothers was only made possible by the construction of an engine that had been specially built to produce a high power output in relation to its weight. While a 180 lb, 15 hp [18] engine may not seem like much in today's terms, however, it was very advanced for its day and helped make possible the first heavier than air flight.

With the advent of jet propulsion systems in the 1940's, thrust per weight ratios were significantly enhanced and a new generation of aircraft was born. Modern technology, while largely based on these early jet propulsion models have developed much further both in high temperature withstanding materials and in combustion characteristics. These improvements are becoming increasingly more important as commercial aviation is becoming an ever more common mode of transportation in the civilian sector and military aircraft are called upon for increasingly better performance. This, coupled with the more stringent requirements for decreased pollutant emissions, has designers looking for revolutionary new combustion and propulsion concepts with which jet engines can continue to increase in performance.

The design process itself has continued to evolve over the years. Until the late 1980's most research done on jet engines was experimental only. However, with the advent and evolution of computers, the feasibility of CFD numerical modeling of entire flow fields, even more complex geometries, is becoming more and more a reality. There are still limitations to what CFD can model, but it can and should be utilized as an essential component to significantly reduce the cost and timeline of the design

process. For example, using CFD on a combustor can allow for the simulation of many different flows and even geometries with minimal cost. Then, as an optimal design or configuration is reached using CFD, an actual physical model can be produced and tested experimentally.

1.2 Conceptual Design

Increasing jet engine thrust output while decreasing the relative weight of the engine is the object of all designers. Much design has gone into materials which can withstand higher temperatures, increasing mixing of the fuel and air, and decreasing the combustor size. In the search for a greater thrust and lighter weight, it is noted that the combustor makes up a significant volume of any jet engine. The reason for this is that combustion takes a finite amount of time and the flow through the combustor is moving quite rapidly. Thus in order to get the energy from the fuel, a combustor must be of a certain length in order to fully burn.

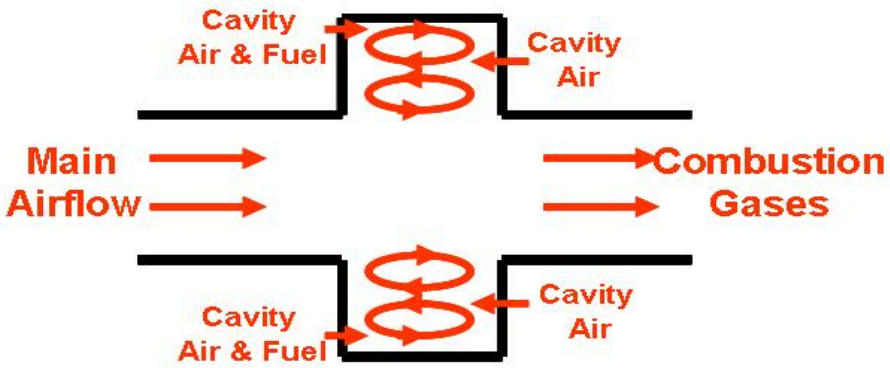

Figure 1.1: Vortex Combustion Concept.

The Ultra Compact Combustor (UCC) offers a different approach that will allow for complete combustion while decreasing significantly the combustor volume. The UCC is based on the Trapped Vortex (TV) concept [12]. This approach included the addition of a recessed cavity in the wall of the combustor in which fuel and cavity air are inserted to stabilize a vortex formed by the main flow shedding off the leading edge of the cavity. One example of a TV configuration is shown in Figure (1.1). Sturgess et

al. [26] determined that a well-designed Trapped Vortex Combustor (TVC) can have superior operability characteristics to a conventional swirl combustor. They defined the term well-designed to include having the right amount of cavity jet air to drive the vortex but to avoid interfacial shear layer burning. This cavity mass flow rate was determined to be approximately 10 percent [26].

The next step in the UCC development was to include the centrifugal-force combustion ideas of Lewis which link flame speed to centrifugal forces incurred by high-G flow [16]. Through his research using a combustion centrifuge, Lewis determined that a reaction will spread through a combustible fuel-air mixture at the fastest of the three flamespreading mechanisms: laminar flame transport, turbulent flame transport, and bouyant bubble transport [15]. Typical flame speeds for these three mechanisms are; laminar (1 ft/sec), turbulent (20 ft/sec), and bouyant bubble (60 ft/sec). Lewis determined that above 500 G's, bouyancy bubble transport becomes the main transport mechanism and that very high centrifugal force fields can be generated with very low pressure losses [16]. By including air inlets at an angle around the circumference of the cavity, a circumferential velocity can be added to the flow inside the cavity in order to produce these centrifugal forces on the fuel-air mixture within the cavity.

The final inclusion in the UCC is the Cavity in a Cavity (CIAC) concept which is a return to the trapped vortex idea. It was noted that as high swirl was added to the combustor, the flame stability gained by the trapped vortex concept was lost. To retain this flame stability, an axially-oriented cavity was inserted in the outer wall of the cavity at each fuel injector location. This shields part of the fuel spray from the high velocity circumferential flows, thus substantially increasing flame blowout velocities.

1.3 Motivation

The UCC design as shown in Figure (1.2) has many possible beneficial applications for the future. These benefits include the obvious increase in thrust to weight ratio, increased flame stability, decreased emissions, increased Mean Time Between

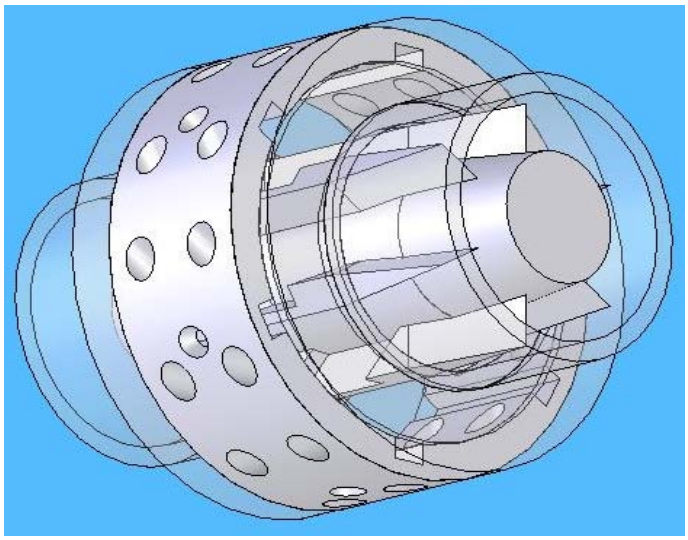

Figure 1.2: Ultra Compact Combustor.

Maintenance (MTBM) and a decreased pressure drop over conventional combustors. Other possible applications such as the inter-turbine burner concept as described by Sirignano and Liu [24] can be made much more feasible due to the decreased combustor size and weight presented by the UCC configuration. According to their research on turbojets, an overall 20 percent increase in specific thrust can be obtained by using inter-turbine burning with only a 10 percent increase in Thrust Specific Fuel Consumption (TSFC), while also lowering the formation of oxides of nitrogen (NO_x) [24]. This decreased combustor weight also makes the UCC design appealing to a myriad of other applications such as for use on UAVs.

Emissions are a topic of concern in today's society. Environmental Protection Agency (EPA) regulations dictate certain emission standards to keep our air clean and safe. There is also an organization specifically geared to setting emission limits for civil aircraft. This organization is the International Civil Aviation Organization (ICAO). The standards set by ICAO are set on a world-wide basis and are specified in terms of the amount of pollutants produced per unit thrust or unit mass of fuel burned. The take-off/landing cycle and the high altitude cruise emissions are given special emphasis [5]. Aircraft engine exhaust has several constituents that are generally considered pollutants. These are smoke (or soot), carbon monoxide (CO), unburned

hydrocarbons (HC), and NO_x. In any aircraft engine, steps must be taken to ensure that the level of pollutant emissions remain within EPA standards [21].

The UCC is designed in such a way as to decrease emissions by more completely burning the fuel in a much smaller volume than a standard combustor. As the fuel and air is swirled circumferentially around the cavity, the high g forces exerted provide for increased mixing, and thus more complete combustion. Also, since NO is produced only in the highest-temperature combustion zones [21], lowering the maximum temperature in the combustor can significantly reduce this harmful emission. Because of the UCC design, the equivalence ratio in the cavity can be quite high, thus allowing the fuel to burn initially at a lower temperature and reducing the ability of NO_x to develop. Then, as the unburned fuel enters the main airflow it burns a second time, again at a lower temperature without allowing NO to develop, while allowing the time and temperature for the carbon monoxide to completely react with available oxygen (O_2), forming carbon dioxide (CO_2) and thereby reducing the carbon monoxide emissions. This is known as Rich Quench Lean Burn (RQL) combustion.

Complete burning is desired not only to protect the environment, but also to increase the thrust output of the combustor. The extent to which the fuel remains unburned is energy lost.

The high temperature of the combustion chamber is a major limiting factor. Materials used in the combustion chamber and its outlet into the turbine are carefully selected to withstand high temperatures, corrosion, and cyclic loading. Even so, these same materials are only able to function with continuous cooling. This is generally done by providing a continuous liner of cool air over the materials which keep them within their operating range even as the combusting and exhaust gases reach temperatures in excess of 2500K [21]. By decreasing weight and using a reheat cycle between the turbines, or an Inter-Turbine Burner (ITB), the UCC design allows for lower combustor temperatures while maintaining the same thrust to weight

ratio. These improvements can substantially increase the MTMB of the combustor and turbine.

1.4 Evalution Criteria

Evaluation of the various combustor designs included several performance parameters evaluated under various air and fuel flow rate conditions. The combustion efficiency (η_b), is the first method of comparing engine efficiencies used in the analysis. The combustion efficiency is calculated using Equation (1.1) where H_C is the heat of combustion for the fuel (43,500 kJ/kg) and $EI_{pollutant}$ is the Emissions Index as defined in Equation (1.2) [3].

$$\eta_b = 100\left[1.00 - 10100\frac{EI_{CO}}{H_C} - \frac{EI_{C_xH_y}}{1000}\right] \tag{1.1}$$

$$EI = \frac{g_{pollutant}}{kg_{fuel}} \tag{1.2}$$

The second comparison was the actual harmful emission levels measured at the exit of the combustor. The majority of gas turbine engine exhaust is made up of carbon dioxide (CO_2), water (H_2O), oxygen (O_2), and nitrogen (N_2). All of these emissions are are generally considered unharmful, although there is some concern of carbon dioxide contributing to the greenhouse effect [5]. However, there are several other emissions that make up a small percentage of the exhaust, yet have very detrimental effects on the environment. The main emissions from aircraft gas turbine engines that are considered harmful pollutants include carbon monoxide (CO), unburned hydrocarbons (HC), and oxides of nitrogen (NO_x). These are generally compared by calculating the number of pollutant particles per million total particles (ppm).

The third criteria for comparison was the pressure drop over the combustor which has a direct impact on the overall efficiency of an engine. The pressure drop

is calculated by dividing the difference between the inlet pressure (P_3) and outlet pressure (P_4) by the inlet pressure as defined in Equation (1.3). To compare the experimental and numerical results, only absolute pressure was used in this calculation. However, for comparison between the numerical grid configurations, both absolute pressure drop and total pressure loss were used.

$$\frac{dP}{P} = \frac{P_3 - P_4}{P_3} * 100 \tag{1.3}$$

There is one other parameter that becomes a limiting factor in combustor performance, albeit indirectly. This parameter is the non-uniform distribution of the exit temperature profile where the exhausted gases hit the turbine, also called hot spots in the flow. A perfect flow would exit in a uniform manner without any hot spots. The profile would have a slight increase in temperature towards the outer perimeter of the flow and the pattern would remain constant with a change in angle. Flows must be kept as uniform as possible because of the temperature limitations on the turbine. When hot spots exist, the average combustor outlet temperature must be lowered to compensate [20].

All CFD analysis was conducted using Fluent, a commercially available CFD program. The validation was conducted using five experimental runs as a baseline and comparing the numerical solutions to the experimental. By applying the correct boundary conditions, as well as turbulent and combustion kinetics in the CFD program, results of all five CFD runs gave results sufficiently close to the experimental runs providing a baseline configuration. The validated numerical model was then applied to four different UCC configurations and compared to the baseline using these same five operating conditions. Comparisons between the experimental and CFD models were made using η_b, species emissions data, pressure drop over the combustor, and by comparing temperature patterns and profiles.

1.5 Research Outline

The trapped vortex and highly accelerated combustion concepts are both beginning to be understood. A working knowledge of how they can interact together, however, especially in a combustion environment, is not yet well understood. How they will work together to affect the combustor performance and how a combustor should be designed to take advantage of their very distinct properties are still unanswered questions. Many studies have been conducted on cannular and annular combustors. But only recently has much work gone into other novel designs, in particular the trapped vortex (TV) and centrifugal force combustor designs. The combination of these concepts opens many possibilities, but there is still much to learn about the design and a knowledge of the consequences of physical alterations to the combustor. Only when the implications of design modifications are known will a consistent procedure to optimize the design be possible.

A functioning UCC has been designed, built, and tested in the laboratory. These experimental tests have been done both at atmospheric and moderate pressures. The next logical step in the design process is to model the flow using CFD. Numerical modeling of the flow using CFD can greatly accelerate the design cycle by modeling the combusting flow through the combustor for several different UCC configurations. This thesis will approach provide a baseline for the design process by modeling the various configurations of the UCC, obtaining numerical predictions as to the pollutant emissions, pressure drop, and temperature profiles for several different cases with each physical configuration, and evaluating the results. From these predictions, decisions can be made as to what physical dimensions should be changed for a desired impact and how the physical geometry of the UCC should be changed for the next UCC physical configuration to be tested in the laboratory.

Several other parameters such as fuel injection droplet size, droplet size distribution, number of injection particle streams, and temperature of injected fuel will be tested to determine their impacts on combustor performance using the CFD models.

Lefebvre lists eleven combustor design requirements which should be met in the design process [14]. Depending on the application, each of these eleven items can have varying degrees of importance. Of these eleven items, four will be used in this paper to characterize combustor performance of the various physical configurations. Combustion efficiency, pressure loss, outlet temperature distribution (pattern factor), and pollutant emissions will all be discussed and analyzed. Others such as the stability limits, durability, and combustion induced flow instabilities will not be analyzed in detail, but are the subject of future work.

II. Background and Theory

2.1 Literature Review

2.1.1 Trapped Vortex. Initial work on the trapped vortex concept was conducted by Little et al. using a cylindrical forebody in a wind tunnel followed closely by a disk afterbody. In their experiments they determined that if the cavity between the forebody and the afterbody had the correct dimensions, then a locked vortex would effectively fill the cavity. This correct cavity size, which in their experiments had an X/D (where X is the cavity length and D is the disk diameter) of 0.6, also corresponds to the minimum drag condition [17].

Hsu et al. then adapted the ideas of Little by conducting an experimental study investigating the use of trapped vortices in cavities as a means of flame stabilization. They concluded that the trapped vortex had good lean blow out (LBO) characteristics, low pressure drops, and combustion efficiencies of about 99% [12].

Hendricks et al. experimentally tested a 12 inch wide rectangular TVC rig that was designed to operate at high inlet temperatures and pressures. The TVC performance data compared favorably with that of conventional combustors [8].

Hendricks et al. also developed numerical CFD models of this rectangular TVC to better understand the flow patterns, specifically the aerodynamics, fuel droplet trajectories, combustion, and exit temperature distributions. This data was compared with the experimental data and was in generally good agreement. In this study a numerical injection droplet size analysis was also conducted [9].

CFD simulation of a cylindrical TVC was conducted using Fluent by Straub et al. to determine the effect of cavity air and fuel injection on vortex stabilization and combustion. They determined that certain vortex phenomena could produce localized high temperature regions on the combustor walls which could lead to increased thermal NO_x [25].

Roquemore et al. also applied the Trapped Vortex Combustion concept to a gas turbine combustor operating under conditions up to 15 atm (220 psi) with

temperatures over 850 K. Using a trapped vortex with a cavity length to depth ratio of 0.6 to stabilize the flame they demonstrated the feasibility of the TVC concept. Their test results indicated that TVC offers a wider operating range, improvements in LBO and altitude relight, and decreased NO_x emission capability as compared to conventional combustors [23].

2.1.2 Centrifugal Force Combustion. Work pertaining to centrifugal force effects on combustion was performed by Lewis. Using a combustion centrifuge Lewis determined that above 500 g, the flame speed is proportional to the square root of the centrifugal force [16]. As a practical application of this manner of increasing flame speed, Lewis then made preliminary efforts to apply these principles to the design of a turbojet afterburner rig [15].

Yonezawa et al. built on the centrifugal force combustion work of Lewis and proposed that there are three ways to acheive combustion loading enhancement. First would be to decrease the mixing time of the fuel and air. Second would be to increase the combustion rate. And third would be to keep to increase the residence time of the fuel and air in the primary combustion zone. Yonezawa et. al. then conducted a numerical study of a jet-swirl combustor which led to the building of a prototype combustor. The efficiencies of this prototype jet-swirl combustor at high loading conditions exceeded those of conventional combustors [28].

Another practical application of the centrifugal force combustion concept of Lewis was done by Anthenien et al. in the construction of the novel, high swirl, Ultra Compact Combustor with an estimated g-loading of about 1000 g. This UCC was constructed for application as both a main combustor and as an inter-turbine burner (ITB). Atmospheric tests were conducted on this UCC with efficiencies above 99% being observed for both ethanol and JP-8 fuels [1].

Numerical analysis of the UCC concept as applied to the ITB has been conducted by Mawid et al. using three dimensional CFD. They determined that the UCC/ITB can operate over a wide range of operating conditions and can achieve

flame lengths about fifty percent shorter than the flame lengths of conventional combustors. They also detemined that to obtain an acceptable temperature profile at the exit, improved mixing is required between the main and cavity air flows [19].

Atmospheric tests have been conducted on the Ultra Compact Combustor as presented by Zelina et al [29, 30] from AFRL/PRTC. However, at high temperature and pressure conditions reactions tend to speed up resulting in shorter flame lengths and much higher combustion intensity. Maintaining a high combustion intensity is important to keeping the engine size small in aircraft engines which because of the combined effects of turbulence, increased flow density, and the fineness of the fuel atomization [11]. Thus a requirement for high temperature and pressure analysis is the next necessary step.

This thesis lays out the experimental and numerical combustion results at high temperature and pressure conditions. Several different operating conditions have been analyzed with the experimental data and compared to the numerical CFD data obtained. Using the flow analyzing techniques available in CFD, a more in depth understanding of essential flow parameters such as the outflow temperature and cavity velocity vectors can be obtained. Using this experimental data and its corresponding numerical model as a baseline, various geometries of the UCC has been constructed and tested, analyzing the flow patterns and determining the effect of several design modifications. All this is an essential step if the UCC is to become a practical reality. If this is to happen, the flow patterns must be understood in order to construct an optimal design that will leverage the obvious advantages of the UCC system without causing any other combustion inefficiencies.

2.2 Emissions

The majority of gas turbine engine exhaust is made up of carbon dioxide (CO_2), water (H_2O), oxygen (O_2), and nitrogen (N_2). All of these emissions are are generally considered unharmful, although there is some concern of carbon dioxide contributing to the greenhouse effect [5]. However, there are several other emissions that make up a

small percentage of the exhaust, yet have very detrimental effects on the environment. The main emissions from aircraft gas turbine engines that are considered harmful pollutants include carbon monoxide (CO), unburned hydrocarbons (HC), and nitrous oxides (NO_x).

Carbon monoxide (CO), is fatal if inhaled in sufficient quantities. It is formed as an integral step in combustion process but most of it reacts to form carbon dioxide (CO_2) before leaving the combustor. However, some carbon monoxide is inevitably frozen in the exhaust as a harmful emission. The reason for this is that the reaction to remove carbon monoxide is most easily done at a high temperature. Thus increasing temperature and residence time in the combustor results in significant decreases in carbon monoxide.

Unburned hydrocarbons are a result of imperfect combustion. They consist of fuel that is emitted in the form of droplets, vapor, or partially oxidized fuel such as methane [14]. Unburned hydrocarbons represent unused energy that went through the combustor. They are considered a pollutant because they may contain carcinogens which have detrimental health effects. They are also considered as harmful to the ozone and contribute to photochemical smog.

Oxides of nitrogen (NO_x) is another pollutant emission. While most NO_x exiting a combustor is in the form of NO, it relaxes in the atmosphere to form NO_2 and is the root cause of smog, the brownish cloud, which has become commonplace in many large cities. They also cause acid rain and ozone depletion at high altitudes [5]. The most important factor for the formulation of nitrous oxides is temperature. Both the combustor inlet temperature and the flame temperature contribute with the flame temperature being the most influential. Increasing residence time in the combustor also contributes by increasing the formation of oxides of nitrogen, however this contribution is minimal when compared to the result of increasing the flame temperature. An increase in flame temperature results in an exponential increase in NO_x formulation [5].

2.3 Temperature Pattern and Profile

Many modern gas turbine engines are limited by the materials from which they are constructed. This is because of the extremely high temperatures that are created in the combustor. In order to extend the life of the combustor walls and turbine inlet vanes while maintaining the combustion efficiency, much research has gone into both the construction of more heat tolerant materials and the design of elaborate cooling systems to maintain the temperature within the allowable range for the materials. This brings out two other very important requirements in combustor design: the temperature pattern and profile.

The temperature pattern is a test of the uniformity of the outlet temperature. In order to get the most efficiency, the outlet temperature should be as high as the materials will allow. However, the material limit is not the average outlet temperature, but the maximum outlet temperature (T_{max}). Therefore good uniformity is important in order to get the average outlet temperature as close as possible to the maximum outlet temperature, thus increasing efficiency as much as possible. The pattern factor is computed as in Equation (2.1), by subtracting the average outlet temperature ($T_{4(avg)}$) from the maximum temperature and dividing this value by the difference between the inlet (T_3) and outlet temperatures. Thus a lower pattern factor is essential to the design of an efficient combustor.

$$PatternFactor = \frac{T_{max} - T_{4(avg)}}{T_{4(avg)} - T_3} \tag{2.1}$$

The temperature profile is the radial distribution of temperatures. It is the ratio of the difference between the maximum circumferential mean temperature (T_{mr}) and the outlet temperature and the difference between the inlet and outlet temperatures as shown in Equation (2.2). As the turbine blades rotate, the way in which they experience the temperature distributed is important. The desired profile is with the peak temperature slightly above the midheight of the turbine blade.

$$ProfileFactor = \frac{T_{mr} - T_{4(avg)}}{T_{4(avg)} - T_3} \tag{2.2}$$

2.4 Inter-Turbine Burner

An ideal thermal engine cycle can be modeled using the Brayton Cycle which consists of four stages: isentropic compression, constant-pressure combustion, isentropic expansion, and constant pressure heat rejection. An analysis of this ideal cycle indicates that the thermal efficiency, η_{th}, of the engine increases as the compressor pressure ratio, τ_c, increases [20]. This is shown in Equation (2.3) where τ_r represents the effects of the flight Mach number, M_0.

$$\eta_{th} = 1 - \frac{1}{\tau_r \tau_c} \tag{2.3}$$

Equations (2.4) and (2.5) show the calculations for τ_c and τ_r. T_{t3} is the total temperature at the combustor inlet, T_{t2} is the total temperature at the compressor inlet, and γ is the ratio of specific heats.

$$\tau_c = \frac{T_{t3}}{T_{t2}} \tag{2.4}$$

$$\tau_r = 1 + \frac{\gamma - 1}{2} M_0^2 \tag{2.5}$$

Thus to increase the efficiency of the aero turbine engine, the compressor ratio has increased significantly to where a τ_c of 30 is common. However, as the combustor inlet temperature increases, the amount of heat addition in the combustor is limited by the physical limitations of the combustor walls. In order to maintain the temperature low enough to not structurally damage the combustor and the turbine inlet, the amount of fuel entering the combustor often must be limited.

Where size and weight are not an issue, as in ground-based gas-turbine engines, this is often bypassed by including a second burn cycle between the high and low pressure turbines. Thus the maximum temperature reached is within the material tolerances, yet the amount of energy added to the flow is significantly increased. This also allows for the option of lowering the maximum temperature through the engine while maintaining the same amount of power output. This can effectively increase MTBM of the engine. The main engineering limitation on turbines is the due to the extremely high temperature gases entering the turbine from the combustor. These temperatures require the turbine blades to be cooled by passing air from the compressor outlet through the turbine blades which has fairly severe performance penalties [20].

Inter-Turbine Burning (ITB) in aero-turbine engines is an area of research that as yet has failed to become a practical reality due to the size and weight constraints placed on aero engines. So, although including a second burn cycle between the high and low pressure turbines can substantially increase the engine efficiencies, the size of the conventional combustor makes the insertion of a second burning cycle impractical. This would increase the size, and therefore the weight, of the jet engine dramatically and offset the benefit gained due to the increased thrust. The decrease in combustor size and weight due to the UCC makes the insertion of an ITB cycle a much more feasible option.

2.5 Heat Transfer

Although combustors are often approximated by assuming adiabatic conditions at the boundaries [20], in order to more closely match the experimental results obtained in the laboratory, it was desirable to take into account some of the heat lost to the surrounding air from the combustor. In order to take this heat transfer into account, radiation and convective heat transfer calculations were made and imposed as boundary conditions for the cavity, inlet, and outlet walls. The emissivity, ϵ, of stainless steel was taken to be 0.85. For the convective heat transfer, calculations of

Table 2.1: Values used in Wall Heat Transfer Calculations

Wall	T_s (K)	T_∞ (K)	D (m)	β (1/K)	ν	k ($\frac{W}{mK}$)	α ($\frac{m^2}{s}$)	Pr
Inlet	500	300	.021	0.0025	26.41E-6	0.0338	38.3E-6	0.690
Cavity	1100	500	.069	0.00125	84.93E-6	0.0573	120E-6	0.709
Outlet	1100	300	.021	0.00143	68.1E-6	0.0524	98.0E-6	0.695

natural convection were made as outlined in Incropera and DeWitt [13] to determine the convection heat transfer coefficient, $\bar{h}$, in $\frac{W}{m^2K}$as shown in Equation (2.6).

$$\bar{h} = \frac{k}{D} N\bar{u}_D \tag{2.6}$$

Where the value for k is a function of the surface and ambient temperatures and as given in Incropera and Dewitt [13], D is the outer diameter of the combustor wall in meters, and the dimensionless Nusselt number $N\bar{u}_D$ is calculated as shown in Equation (2.7).

$$N\bar{u}_D = \left[0.60 + \frac{0.387 * Ra_D^{\frac{1}{6}}}{\left[1 + \left(\frac{0.559}{Pr}\right)^{\frac{9}{16}}\right]^{\frac{8}{27}}} \right]^2 \tag{2.7}$$

Where the dimensionless Prandtl number, Pr, is a function of the temperature (for these cases $Pr = 0.7$) and the Rayleigh number, Ra, is calculated from Equation (2.8).

$$Ra = \frac{g\beta(T_s - T_\infty)D^3}{\nu\alpha} \tag{2.8}$$

The values for the volumetric thermal expansion coefficient (β), kinematic viscosity (ν), and thermal diffusivity (α) are all functions of the wall surface temperature (T_s) and ambient temperature (T_∞) and are also given in Incropera and Dewitt [13]. The constant g is the acceleration due to gravity in $\frac{m}{s^2}$.

The values used for these calculations are given in Table (2.1).

2.6 Computational Fluid Dynamics

Computational Fluid Dynamics (CFD) began in earnest in the early 1970's. Its basic premise is to use spatial and temporal discretization techniques to solve the governing fluid dynamics equations over a given flow field. Any discretization scheme has inherent discretization error [4]. While discretization errors cannot be completely eliminated they can and must by reduced to within the allowable accuracy for a given problem. Several variables can be adjusted, such as decreasing the spacial and temporal step sizes, to reach an accurate solution. The obvious limitation to this approach is the computing power and time available. For this reason, the evolution of CFD continues to be inextricably linked to the evolution of computers.

2.6.1 Relaxation Parameters. Successive overrelaxation (SOR) is a common numerical technique used to accelerate solution convergence by observing the change of a given parameter between successive iterations, noting the direction of change, and predicting that the same trend will continue into the next iteration [27]. In this manner, solutions can be converged upon more quickly with less computational expense. This technique requires the use of an arbitrary relaxation parameter, ω, which can be varied to acheive the greatest convergence rate for a given flow field. For most simple flow fields overrelaxation will yield a much faster solution. However, in more complex flow fields, overrelaxation causes the solution to be continually overshot, resulting in a high number of oscillations which take time to damp out. Occasionally these oscillations will never damp out unless underrelaxation is implemented. Underrelaxation helps to dampen out the oscillations and help solution convergence.

2.6.2 Turbulence Modeling. Turbulence flow is difficult to model due to the apparent irregular motions and lack of closure of the governing equations. While it is generally considered to be governed by the unsteady Navier-Stokes equations, the difficulty involved in acheiving a direct numerical simulation (DNS) due to the extremely small length and time scales required is above the ability of our current computer resources except for relatively simple flows at low Reynolds numbers [27].

Thus it is necessary to use time or spacial averaging such as in the time-averaged Reynolds Averaged Naver-Stokes (RANS) equations and to model turbulence using assumptions about the turbulent stress and heat flux quantities.

Turbulence models from the simplest of zero-equation models to the more exact and computationally intensive Large Eddy Simulation (LES) model [4]. All these models have certain characteristics. Some are good for boundary layer calculations yet fall short in the wake regions. Others have properties which enable them to model flow in wakes, shocks, or other fluid flows which may be encountered. Because all turbulence models have limitations it is imperative to choose the model which will provide reasonable accuracy for the specific flow field which is being modeled.

Modeling of turbulent flow becomes very difficult near the wall in the viscous sublayer. In order to adequately compute the flow field in this area the mesh must be very refined. In many cases this increase of refinement near the walls is not feasible. In these cases the use of wall functions is common practice. Many turbulent flows have shown a universal behavior in the viscous sublayer. Wall functions take advantage of this commonality and serve as a bridge between the wall and the inner turbulent flow. This bridge between the wall and the vicous flow within the domain can be made without significantly reducing the accuracy of the results for attached boundary layers [4]. Wall functions also significantly decrease computational intensity and the procedure has become very well developed for models such as the k-ϵ model [27]. The k-ϵ model is a widely employed two-equation eddy-viscosity model which is based on the solution of equations for the turbulent kinetic energy and the turbulent dissipation rate [4].

2.6.3 Species Modeling. There are three basic models for chemically reacting gas mixtures. The first is to consider the flow to be frozen, or non-reacting. This is appropriate for flows where the residence time is much less than the time required for reaction, or the reaction rate. Hypersonic flows frequently use the frozen assumption in calculations.

The second model is much more difficult. It considers the reaction to be a rate controlling process. In this model, the chemical kinetics for all the pertinent constituent species must be taken into account. A good comprehensive model that considers the reaction kinetics involved can be very computationally expensive. This is especially pertinent in a complex flow such as a combustor where implementation of this model would involve many tens of species and hundreds of reactions which must be evaluated for each cell and at each time step.

The third basic model is to consider the flow to be in chemical equilibrium. In this case it is assumed that the reaction time is short with respect to the residence time. A chemical equilibrium model assumes that equilibrium for a given species set is reached at each point in the flow. This model is sometimes referred to as mixed-is-reacted in fuel flows because at each point in the flow where the oxidizer and fuel reach the required reaction concentrations, combustion takes place and an equilibrium state is reached. It is generally a good approximation for performance estimates of combustors to assume the burned gases produced by the combustion process to be in chemical equilibrium [10].

2.6.4 NO_x Modeling. NO_x emission formulation in combustion systems are of three types; thermal, prompt, and fuel NO_x. Fuel NO_x is a product of the nitrogen which is bound into the fuel which is generally between 0.3 and 2 percent. Fuel NO_x is generally more prevalent in diesel fuels than in aerospace fuels.

The formation of thermal NO_x is highly temperature dependent. It is generally modeled using highly temperature-dependent formulas such as the extended Zeldovich mechanism. Prompt NO_x however, are most prevalent in rich flames and generally is only significant in cases where the flow is fuel rich, low temperature, and/or residence times are short. In computational modeling, the variation in NO_x can generally be accurately predicted although the exact quantity itself cannot always be pinpointed [6].

III. Experimental Configurations

3.1 Experimental Procedure

3.1.1 Experiments. The experimental analysis of the UCC at high temperatures and pressures was conducted by AFRL/PRTC. It was conducted in the high pressure facility in Building 18 on Wright Patterson AFB. The physical combustor was run using a variety of temperatures (T), pressures (P), mass flow rates of main and cavity air flows ($\dot{m}_{main}$ and $\dot{m}_{cavity}$) and equivalence ratios (Φ) to simulate as closely as possible the conditions of actual use. The conditions of each of these runs are shown in Table (3.1).

Experimental tests on the UCC were run using JP-8+100 fuel, a military kerosene-based fuel with a thermal stability package. Fuel injection was done at six equally spaced points around the circumference of the main cavity inside of the axial recessed cavity. Fuel was injected using pressure-atomizing nozzles with a Sauder Mean Diameter of approximately 55 microns, a Flow Number (FN) of 0.5 for each injector (total rig FN =6), and a half cone angle of 35 degrees. The Suater Mean Diameter (SMD) is the diameter of a drop with the same surface/volume ratio as the mean value of the spray [5].

Around each fuel injector, outside of the axial recessed cavity, were four cavity air inlets angled at a 37 degree angle to produce the cavity fuel-air mixing and circumferential flow leading to a high centripetal acceleration of the flow.

Emission testing was done just downstream of the trailing edge of the six vanes. In order to get an accurate reading, four sensors were inserted into the flow at uniform

Table 3.1: Experimental Run Conditions

Run	$\dot{m}_{main}(\frac{lb}{min})$	$\dot{m}_{cavity}(\frac{lb}{min})$	P(psia)	$\frac{dP}{P}(\%)$	T (F)	overall Φ	cavity Φ
1	29.1	6.4	41.2	4.7	491	0.294	1.620
2	29.7	6.2	49.4	3.0	515	0.289	1.677
3	65.0	12.7	59.2	8.2	530	0.147	0.899
4	50.6	12.2	62.3	4.9	475	0.172	0.888
5	29.6	7.8	61.1	2.8	526	0.338	1.621

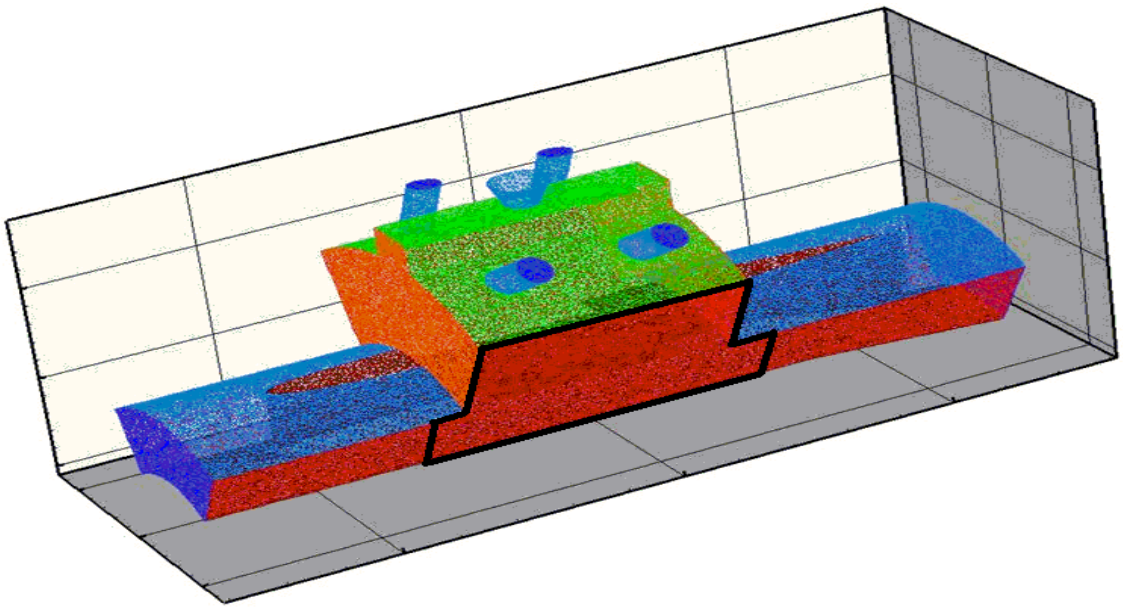

Figure 3.1: Ultra Compact Combustor Numerical Mesh.

increments and the results were averaged to get the readings for the CO, CO_2, O_2, NO_x, and HC.

Static temperature and pressure were measured at two separate locations on the circumference of the combustor and averaged. This was done to monitor the temperature and pressure at both the inlet and outlet.

3.2 Numerical Procedure

The current design of the UCC can be sectioned into six equal periodic sections, each cross-sectional area in the shape of a slice of pie. Each of these sections consists of its portion of the inlet, outlet, four cavity flow inlets, and a fuel injector. With the effect of gravity assumed to be negligible, the CFD analysis of the UCC was done on one section of the physical geometry as shown in Figure (3.1). The portion of the red periodic boundary outlined in Figure (3.1) is depicted in several figures throughout the report.

The selected CFD model used thoughout the validation and optimization processes was Fluent. The solver used was segregated and implicit using a $k-\epsilon$ turbulence

model with wall functions. A non-premixed, 11 species, equilibrium combustion model was used. In all cases the steady state solution was computed.

3.2.1 Grid Construction. Grid construction consisted of two phases: the geometric construction in Solidworks, and the usage of these geometric parameters to form a grid in Gridgen. Solidworks CAD models of the UCC and various alternative configurations of the Ultra Compact Combustor were constructed. These were each then saved as an IGES file. Gridgen was then used to convert the UCC physical configurations drawn from the IGES file into a three dimensional unstructrured, tetrahedral mesh which could be used to model the flow through the combustor. After constructing the grid and setting the initial boundary conditions and fluid parameters, the grid was exported as a case file to Fluent on which the CFD analysis could be completed. The mesh used for Geometry 1 is shown in Figure (3.1).

Five different UCC configurations were tested numerically. The first configuration, Geometry 1, was identical in geometry to the UCC tested experimentally. Comparison with the experimental data was done using Geometry 1 in order to validate the model. Geometry 1 will also be referred to as the baseline configuration. Geometries 2, 3, and 4 maintained much the same configuration with only slight geometric differences as outlined in Table (3.2) where A_3 and A_4 are the combustor inlet and outlet areas respectively and D_{jets} is the diameter of the cavity air jets in inches . These were used to test the impact of increased outflow area, decreased cavity circumferential velocity, and decreased cavity length respectively. The final grid, Geometry 5, was used to evalute the vane curvature on the engine performance. This grid maintained the configuration of the decreased cavity length with the addition of 0.2 radians curvature to the vane.

3.2.2 Species Modeling. As stated earlier, the three basic methods of species modeling are frozen, equilibrium, and rate-controlling flows [10]. Of these three the most practical, due to its relative computational ease and sufficiently good accuracy, for modeling the combustion process in a subsonic combustor is to use the equilibrium

Table 3.2: Numerical Grid Geometries (*Geometry 1=Baseline Configuration)

Model	$\frac{A_4}{A_3}$	D_{jets}	Cavity Length	Vane Curvature	# Cells
*Geometry 1	1	0.213 (in)	1.875 (in)	0 (rad)	271000
Geometry 2	1.264	0.213 (in)	1.875 (in)	0 (rad)	243000
Geometry 3	1	0.426 (in)	1.875 (in)	0 (rad)	432000
Geometry 4	1	0.213 (in)	1.50 (in)	0 (rad)	262000
Geometry 5	1	0.213 (in)	1.50 (in)	0.2 (rad)	249000

assumption. This sort of chemistry is often referred to as mixed-is-reacted and was assumed in all computations of species mole fractions. Eleven chemical species were considered in the combustion process using a probability density function (PDF). These species are $C_{12}H_{23}$, CH_4, CO, CO_2, H_2, H_20, H_20(liquid), 0_2, OH, C(S), and N_2. This PDF was created using prePDF software for each individual operating condition and read into Fluent to solve the chemical equilibrium at each phase in the combustion process.

Postprocessing of the species data was done on a mole basis by taking the percentage of each individual species directly as a Fluent output. The extraction of the unburned hydrocarbons required more effort. In Fluent, the unburned fuel droplets that escape the domain are not included in the species data given, only the evaporated fuel is included. Also, because of the equilibrium chemistry model, most evaporated hydrocarbons were combusted shortly after evaporation making for only a very small mole percentage of hydrocarbons in the exhaust. Therefore, it was necessary to calculate the mole percentage of unburned liquid hydrocarbons from the concentration of the unburned droplets, the density of the exhaust air, and the molar masses of the constituent species and add that to the evaporated hydrocarbons given in the output. This calculation is shown in Equation (3.1) with the molecular mass (MM) of the exhaust calculated to be about 28.8 g/mol.

$$ppm_{HC} = ppm_{vapor} + \frac{\frac{\rho_{HC_{fluid}}}{MM_{HC}}}{\frac{\rho_{exhaust}}{MM_{exhaust}} + \frac{\rho_{HC_{fluid}}}{MM_{HC}}} \tag{3.1}$$

3.2.3 Operating Conditions. Several parameters are important in the construction of the PDF model, one of which is the inclusion of the proper operating conditions. This is essential especially at high temperature and pressure operating conditions because Fluent reads in the operating conditions from the PDF file. These condititions are then used to calculate other flow parameters. For example, when Fluent reads in the PDF it uses the operating pressure given to calculate the density at each point in the flow by using the ideal gas law as shown in equation (3.2). The operating pressure must accordingly be set at an average value of the inlet and outlet pressures to correctly model the flow.

$$\rho = \frac{P_{op}}{RT} \tag{3.2}$$

The operating condition that will have the most impact between these runs is the operating pressure. As is shown in Table (3.1), the operating temperatures vary from about 475 to 530 degrees Fahrenheit which with a set pressure in an ideal gas leads to a density variation of about $0.1\ \frac{kg}{m^3}$. The operating pressures vary from 39 to 59 psia which with a set temperature leads to a density variation in about $1\ \frac{kg}{m^3}$. Due to the importance of density to the flow velocities and other characteristics, it can be expected that pressure variation between cases will have more of an impact than the temperature variations.

3.2.4 Pollutant Modeling. Thermal and Prompt NO_x were both modeled in these experiments. Because of the dependence of NO_x formulation on the flow environment, it can be modeled after the flow is developed as a post-processing task. Fluent modeled them in this manner, determining the thermal NO_x formation using the highly temperature dependent extended Zeldovich mechanism, with the rate constants based on numerous experimental studies [6]. The principle reactions governing the fomation of thermal NO_x from N_2 as utilized in the extended Zeldovich mechanism are given in Equations (3.3) to (3.5) where R is the Universal Gas Constant [7].

$$O + N_2 \rightleftharpoons NO + N \qquad k_f = 2 * 10^{14} exp(-315/RT) \tag{3.3}$$

$$N + O_2 \rightleftharpoons NO + O \qquad k_f = 6.4 * 10^{9} exp(-26/RT) \tag{3.4}$$

$$N + OH \rightleftharpoons NO + H \qquad k_f = 3.8 * 10^{13} \tag{3.5}$$

The prompt NO_x was similarly modeled from a complex series of reactions resulting in fuel fragmentation and NO_x formulation using the equivalence ratio and number of carbon atoms per fuel molecule as inputs. Because the fuel used in all cases was the same and the percent of N_2 bound in the fuel was unknown, the fuel NO_x was not taken into account for these experiments. It can be reasonably assumed that while a slight decrease in NO_x may result, the comparison of increasing or decreasing NO_x trends would not be significantly altered due to this omission.

The majority of NO_x exiting combustors is nitric oxide (NO). The maximum percentage ratio of $\frac{NO_2}{NO}$ for JP-8 type fuels is about 2 percent [10]. Therefore, for these models only the NO emission will be included in the total mole fraction of NO_x given.

3.2.5 Turbulence Modeling. Turbulence in the flow was modeled using a standard k-ϵ turbulence model and standard wall functions as contained in Fluent. The k-ϵ model is perhaps the most widely used two-equation eddy-viscosity model. It offers a reasonable compromise between accuracy and the computational intensity of the solution for a wide variety of flows including wakes, jets, and mixing layers. This is important in the flow through the UCC due to the mixing layer created by the cavity and main airflow interaction.

3.2.6 Fuel Injection. The fuel used in the combustor was modeled using kerosene, $C_{12}H_{23}$, due to its similar thermodynamic properties to the JP-8+100 fuel

used in the experiments. Several parameters are important for the inclusion of fuel injection in a combustion model. Some of the parameters which were considered in order to more closely match the experimental procedure are the droplet size and distribution, injection profile, and inlet velocity.

Residence time required for complete droplet evaporation and combustion is inextricably linked to the droplet diameter as described in the d^2 Law [7]. Numerical tests of various droplet sizes indicate a large drop in combustor efficiency as the droplet diameter passes the point where the droplet can completely combust before exiting the combustor.

Five hollow cones at varying cone angles and droplet sizes were injected at 30.5 m/s into the flow. They were set up to model a 35 degree half cone angle with a mean droplet diameter of 55 microns.

3.2.7 Boundary Conditions. Once the physical geometry and operating conditions are established, the next objective is to match the boundary conditions as closely as possible to conditions experienced by the actual physical combustor. Only then will the flow through the combustor be modeled correctly. On the CFD model of the UCC combustor, there were three main boundaries; the air flow inlets (both the main and cavity inlets), the outlet, and the walls.

3.2.7.1 Inlets. In order to match the experimental results, it was necessary to set the main airflow and cavity inlets as mass-flow inlets. With the injector also set to deliver a specified mass flow rate of fuel, the equivalence ratio was fixed to match the experimental runs. Also important to the solution was defining a total temperature of the inlet flow equal to the experimental inlet total temperature. The pressure at the main and cavity jet inlets were not set in order to not overconstrain the system. The inlet pressures were taken as an output and used in the pressure drop calculations.

3.2.7.2 Outlet. The outlet boundary condition became very important in these high pressure and high temperature models. In order to maintain the pressures evident in the experimental runs, the outlet boundary condition was set as a pressure-outlet. The set pressure at the outlet was the difference between the operating pressure, P_{OP}, and the atmospheric pressure as shown in Equation (3.6) to get the gauge pressure. The outlet temperature was then set to a temperature close to the adiabatic flame temperature of the fuel at the equivalence ratio of the run. This outlet temperature is only used in instances of backflow into the combustor.

$$P_{gauge} = P_{op} - P_{atm} \tag{3.6}$$

3.2.7.3 Walls. Wall boundary conditions set in the CFD model of the UCC include sections of heat transfer, adiabatic, and periodic boundary conditions.

Adiabatic (no heat transfer) boundary conditions were applied to the vane and inner diameter walls where heat transfer is negligible due to the symmetry of the physical combustor.

The adiabatic assumption is frequently made when modeling combustors. However, in order to more closely approximate the results from the experimental runs, heat transfer was accounted for on both the inlet and exit walls, front and rear flanges, and in the cavity. The heat transfer boundary conditions were applied using a heat transfer coefficient and and emissivity parameter in conjunction with the wall thickness. The emissivity parameter is a property of the wall material which in the experimental case was stainless steel with an emissivity, ϵ, equal to 0.85.

The heat transfer coefficient is a function of the wall and ambient temperatures and was calculated separately for the cavity, flanges, and inlet and exit walls using the natural convection assumptions and calculations as outlined in Incropera and DeWitt [13] and discussed earlier. The inlet and exit wall heat transfer coefficients were calculated to be 10.2 and 12.1 $\frac{W}{m^2K}$ respectively with the cavity and flange coefficients set at 8.1 $\frac{W}{m^2K}$. The farfield temperature for the inlet wall, flanges, and

exit wall were approximated at 300K and for the cavity, which is enclosed, was set at 500K.

The periodic boundary conditions were applied on the faces of the UCC model which would be attached to the adjoining section of the combustor. Since each section is identical in function, the properties of the flow leaving one face can be modeled as entering the adjoining face.

IV. Results and Discussion

4.1 Validation of CFD Model

Validation of the numerical model was done by comparing the numerical results of Geometry 1 with the experimental results from five individual runs at various temperatures, pressures, and equivalence ratios. Geometry 1 modeled the current experimental configuration of the UCC and became the baseline for comparison for the other designs. The conditions of each of these runs is outlined in Table (3.1) and were constructed in such a manner as to model a variety of the conditions which the combustor would be subjected to throughout a typical mission. For each of the cases, the boundary conditions were set to replicate the experimental setup. Table (4.1) compares the experimental data with the numerical predictions. Comparisons between the CFD and experimental were made using species emissions data as well as the temperatures, combustor efficiency (η) and pressure drop over the combustor.

Table 4.1: Comparison of Experimental vs Numerical Results

Run	$\frac{dP}{P}(\%)$	CO(ppm)	$CO_2(\%)$	$O_2(\%)$	NO_x(ppm)	T_{exit}(K)	$\eta(\%)$
1 - Exp	5.0	1089	3.2	16.4	37.3	1254	97.5
1 - Num	4.4	997	5.2	12.8	64.4	1408	96.0
2 - Exp	3.3	1264	3.7	15.7	48.2	1256	97.7
2 - Num	3.6	1016	5.1	12.8	59.0	1402	95.2
3 - Exp	8.3	478	1.6	18.7	15.6	931	98.0
3 - Num	9.8	454	2.6	16.8	18.1	1026	95.2
4 - Exp	5.1	524	2.3	17.7	27.3	965	97.9
4 - Num	6.8	424	3.0	16.2	19.9	1084	95.7
5 - Exp	3.0	1962	4.3	14.9	58.9	1366	96.4
5 - Num	3.6	1334	5.8	11.8	88.5	1508	96.6

The pressure drop comparison between the numerical simulations and the measured experimental data shows, with the exception of run 1, a numerical pressure drop between 8 and 17 percent lower than the experimental data. Run 1, which has a total mass flow rate of 35.5 $\frac{lbm}{min}$ at an inlet pressure of about 41 psia, is the lone run in which the experimental data shows a larger pressure drop than the numerical results. However, the pressure drop difference between the numerical and experimental is still within an acceptable margin of less than 12 percent.

The CO_2 and O_2 data are directly related to the combustion process. The O_2 is the oxidizer in the combustion process and enters the combustor at approximately 21 percent mole fraction of the total flow. As it reacts with the hydrocarbons, water and CO_2 are the main products formed. Thus the levels of CO_2 and O_2 are inversely proportional and are indicators of how much fuel has been combusted. Numerical combustion models such as the one resident in Fluent generally use an equilibrium model, often refered to as mixed-is-reacted. In these models, if a mixure of fuel and oxygen are mixed in the right proportions and conditions they are considered to be instantaneously converted to their equilibrium state. Thus it is not surprising that the numerical data shows a more completely combusted state with higher concentrations of CO_2 and lower concentrations of O_2. Considering the assumptions made in the combustion modeling process, the numerical and experimental data compares quite nicely.

The CO emissions calculated in the numerical tests are very close to those obtained by the emissions probe in the experimental tests. The numerical results as shown in Table (4.1) are all slightly lower than the experimental data. This difference margin decreases as the CO quantity decreases. This is another indication that the equilibrium model would tend to more completely react than actual experiments might show. The numerical CO emissions data for cases 1 through 4 are all within 20% of the experimental CO results. Run 5, which has a total mass flow rate of only 37.4 $\frac{lbm}{min}$ and a relatively high inlet pressure of over 61 psia, has the highest amount of CO emissions for both the experimental and numerical tests and the biggest percentage difference between the two at 32 percent.

Exact matches between the experimental and numerical results were not imperative. However, it was necessary that the numerical model follow the trends of the physical experiments. The pressure drop, CO, CO_2, O_2, and NO_x all match sufficiently well between the CFD and Experimental runs. But even more importantly, the trends between cases are very clear, serving as validation that the model can ful-

fill its purpose to depict trends of increasing or decreasing emissions, efficiencies, exit temperatures, and pressure drops between UCC configurations.

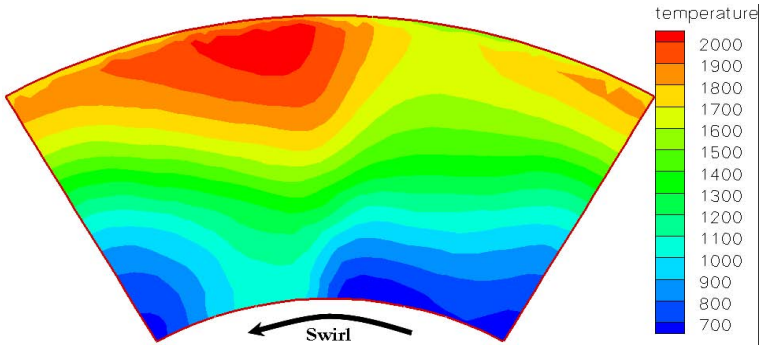

Figure 4.1: Run 1 Temperature Contours at Outlet of Experimental Configuration (Geometry 1)

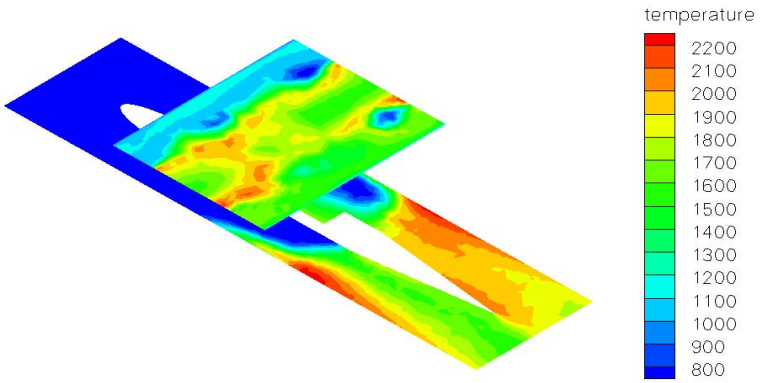

Figure 4.2: Run 1 Cutaway Temperature Contours of Experimental Configuration (Geometry 1)

One major benefit of CFD is the ability to get inside the flow field. As discussed earlier, the pattern temperature profile at the exit plane where the flow enters the turbine and hot spots located near combustor walls is very important. Figures (4.1) and (4.2) show the temperature contours at the exit plane and on two horizontal planes in the original configuration of the UCC, respectively. The temperature at the exit plane as shown in Figure (4.1) looking out from the combustor is not very uniform and will need to be improved before implementation of the UCC in a gas turbine engine. The contours of this original configuration will be compared with

the various other configurations tested in order to determine the impact of design modifications on the temperature patterns inside the flow of the UCC.

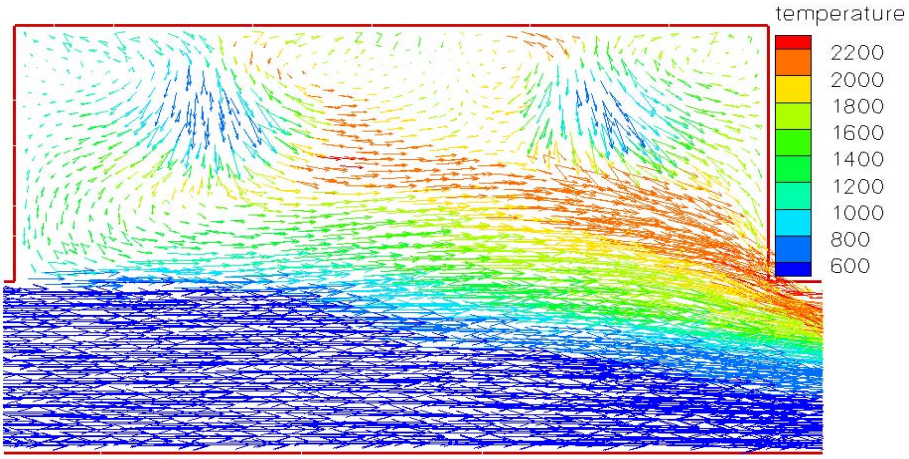

Figure 4.3: Cavity Velocity Vectors of Baseline Configuration (Geometry 1) on Periodic Boundary (Run 1)

Figure (4.3) shows the velocity vectors colored by temperature contours of the experimental configuration at the periodic plane of the numerical mesh. This corresponds to the plane oriented radially from the combustor center and axially between the fuel injectors. These show that when the main cold airflow comes by the cavity, some of the air is shedded off and mixes into the cavity. Likewise, the cavity high temperature air is located about midway up the cavity starting about midway into the cavity length. This temperature stratification within the cavity is indicative of the way the cold, dense, unreacted particles are flung by the centrifugal forces to the outer wall of the cavity while the hot, less dense, reacted species move toward the center of the combustor. The combustion process continues as shown by the high temperatures in the mixing plane as the cavity and main air flows mix and the flow exits the combustor.

Another indication from Figure (4.3) is that the cavity length may be more than sufficient. The high temperatures do not begin until halfway through the cavity with a large portion of the cavity filled with colder species. If comparable combustor

Table 4.2: Baseline(Geometry 1) vs Increased Outflow Area Configuration(Geometry 2) Emission and Efficiency Comparison

Run	CO(ppm)	CO_2(%)	O_2(%)	NO_x(ppm)	HC(ppm)	η(%)
1 - Geometry 1	997	5.2	12.8	64.4	100	96.0
1 - Geometry 2	1585	4.6	13.6	103.6	196	92.6
2 - Geometry 1	1016	5.2	12.8	59.0	124	95.2
2 - Geometry 2	1780	4.6	13.5	108.7	208	91.9
3 - Geometry 1	454	2.6	16.8	18.1	66	95.2
3 - Geometry 2	467	2.3	17.3	22.4	106	92.8
4 - Geometry 1	424	3.0	16.2	19.9	70	95.7
4 - Geometry 2	484	2.5	17.0	26.0	119	93.2
5 - Geometry 1	1334	5.8	11.8	88.5	84	96.6
5 - Geometry 2	964	4.3	14.1	64.5	168	94.8

efficiency could be achieved with a decreased cavity length it would be a considerable advantage.

4.2 Impact of Increased Outflow Area

With the validation of the CFD model under this array of conditions, another configuration of the UCC was analyzed. This configuration, (see Geometry 2 in Table (3.2)), was identical in geometry to the previous model except for the discharge area being increased by 26.4 percent. The goal of this comparison was to determine if a larger discharge area would be effective in reducing back pressure in the combustor while maintaining low emissions. A reduction in pressure drop over the combustor is coverted directly to drag savings for the aircraft because all pressure losses directly increase the drag. The results for this modification on emissions, pressure drops, and temperature profiles are compared with those of the baseline (or original) configuration, Geometry 1, in Tables (4.2) and (4.3).

4.2.1 Efficiency and Emissions Impact. Run 1 has a total mass flow rate of 35.5 $\frac{lbm}{min}$ and an inlet pressure of 41 psia while run 2 has a similar mass flow rate of 35.9 $\frac{lbm}{min}$ with a higher inlet pressure of 49 psia. In both of these runs, the increased outflow area configuration exhausted significantly more pollutant emissions, both CO

and NO_x, than the baseline configuration. Thus the efficiency of the increased outflow area UCC is significantly decreased from that of the baseline. This is in all probability directly linked to the outflow area increase which resulted in decreased residency time, and thus decreased combustion, in the combustor.

It was also noted that under these conditions the numerical simulation of the increased outflow area UCC had a more difficult time converging. These convergence difficulties are likely a result of backflow from the outlet back into the combustor exit. While backflow for a few cells was evidenced in several of the UCC configurations, this configuration had the greatest amount of backflow from about 4-7% of the outlet cells. This non-uniform velocity profile at the exit is not desireable and some modifications should be made to make the flow exit more uniformly. This flow uniformity is a part of the optimization process for the UCC and modification ideas will be discussed throughout the next two chapters. Figure (4.4) shows the velocity contours at the outlet, looking into the combustor, for the increased outflow area configuration. Take note of the negative velocities on the lower right where the backflow occurs.

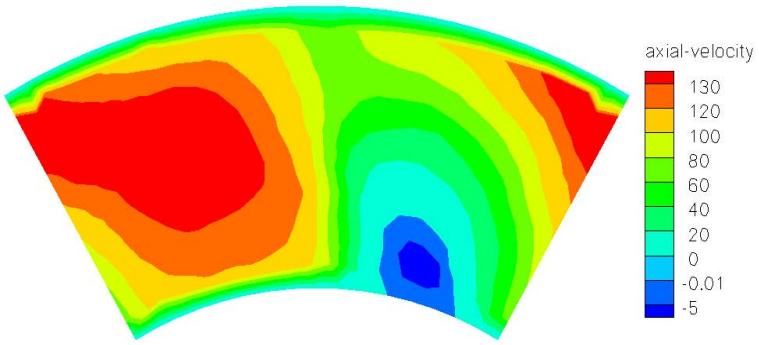

Figure 4.4: Run 1 Outlet Velocity Contours of Increased Outflow Area (Geometry 2)

Under higher pressure conditions the increased outflow area configuration performed better than in the previous two low pressure runs. At higher pressures and mass flow rates, such as in run 3 where the total mass flow was increased to nearly 78 $\frac{lbm}{min}$ and the inlet pressure was increased to 59 psia, and run 4 with a mass flow rate of 63 $\frac{lbm}{min}$ and an inlet pressure of 62 psia, the pollutant emissions and combustor

efficiencies are within 2-3 percent of the original configuration. The final set of operating conditions, run 5, which has a high operating pressure (61 psia) with a relatively low mass flow rate (37 $\frac{lbm}{min}$), the increased outflow area UCC configuration shows a significant decrease in CO emissions. The efficiency in this run is still a couple percentage points off the efficiency of the original configuration, however, the majority of the efficiency losses in both runs is due to the escaping unburned hydrocarbons.

The primary reason for the decreased combustion efficiencies in the increased outflow area configuration is the large amount of unburned hydrocarbons exiting the combustor. This value ranges from 61 to 100% over the baseline configuration with an average increase of 79% for these five cases. With decreased droplet sizes it is possible that the increased outflow area configuration might be an option for high pressure flows.

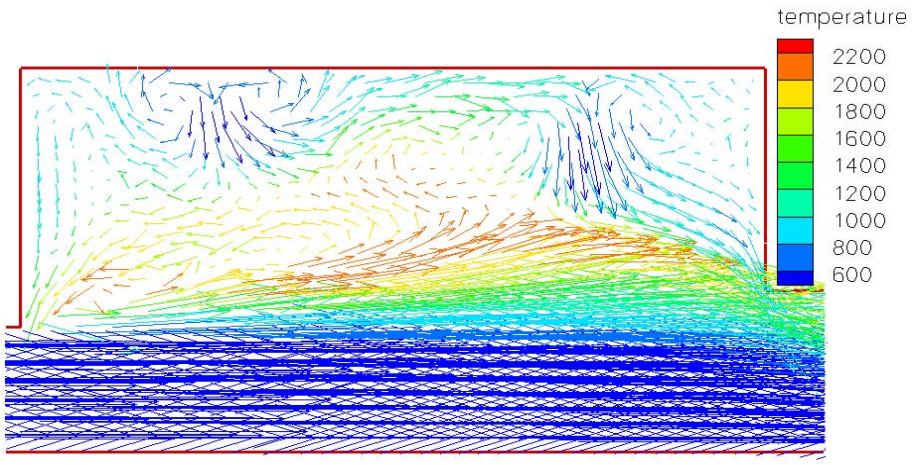

Figure 4.5: Cavity Velocity Vectors of Increased Outflow Area (Geometry 2) on Periodic Boundary (Run 1) *Note the increased outer diameter of this configuration as the flow exits the cavity.

4.2.2 Cavity Velocity Profiles. One of the reasons for the reduced efficiency of the increased outflow area configurations is shown in Figure (4.5) which is a velocity vector plot contour colored by temperature. Comparison with Figure (4.3) shows a much smaller high temperature area in the increase outflow area. It also appears that the combustion process is significantly slowed as it enters the main airstream.

This may account for the 75% increase in unburned hydrocarbon emissions over the baseline configuration and the low combustion efficiency. By comparison, the baseline configuration maintains high temperatures, indicative of combustion, as it exits the cavity and enters the main air flow.

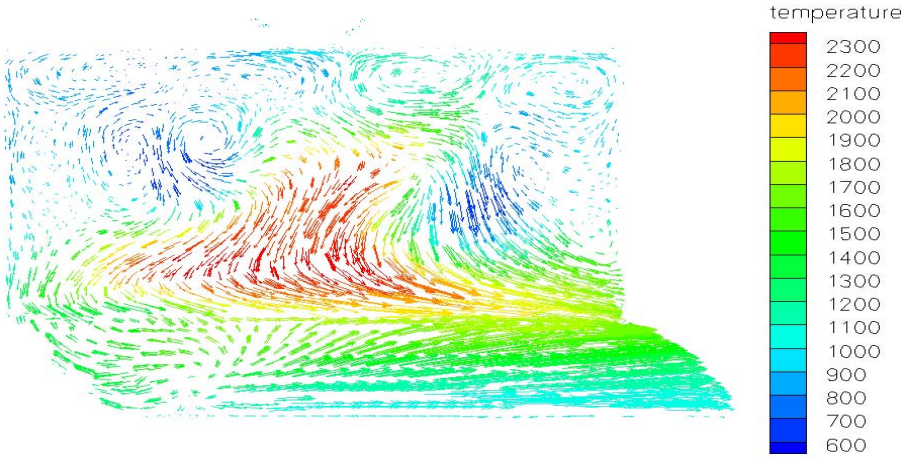

Figure 4.6: Cavity Velocity Vectors of Increased Outflow Area (Geometry 2) through Cavity Area on Fuel Injector Plane (Run 1)

Figure (4.6) shows a similar profile, except the contour plane is aligned radially with the fuel injector plane as opposed to between the fuel injectors. The basic pattern of flow remains unchanged with the high temperature area more tightly compacted when aligned with the injector. As the flow moves circumferentially, the high temperature areas descend toward the centerbody and spread out to fill more of the cavity allowing the cold, unreacted air to fill in near the cavity outer wall.

This stratification of the cold and hot gases within the cavity due to the high centrifugal forces is further shown in Figure (4.7) which is a cross-sectional plot of the cavity velocity vectors colored by temperature contours.

4.2.3 Pressure Loss Comparison. Static pressure drop for the increased outflow area configuration was decreased for each operating condition. However, an even more applicable measure of performance between this and the baseline configuration due to the increased outflow area is the total pressure drop which takes into account the flow velocity magnitude. For the increased outflow configuration (Geometry 2),

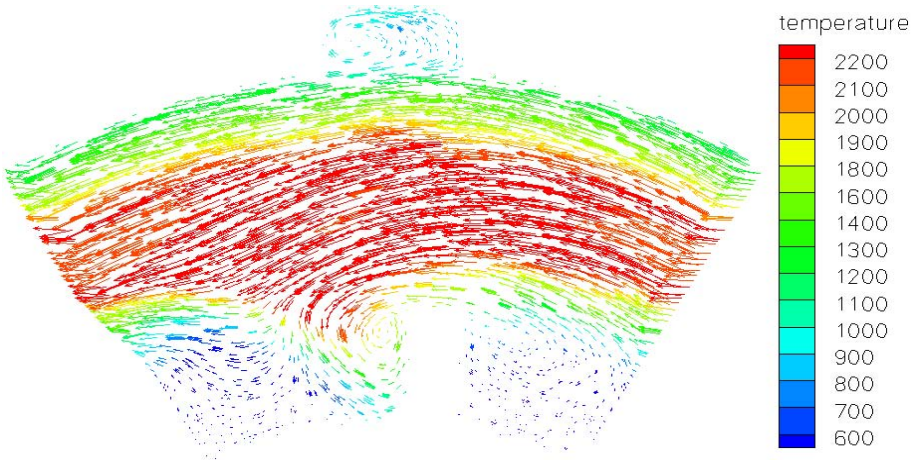

Figure 4.7: Run 1 Cross-Section Velocity Vectors of Cavity Area for Increased Outflow Area Configuration (Geometry 2)

Table 4.3: Baseline(Geometry 1) vs Increased Outflow Area Configuration(Geometry 2) Pressure Loss and Pattern Factor Comparison

Run	$\frac{dP}{P}_{abs}$ (%)	$\frac{dP}{P}_{total}$ (%)	Pattern Factor
1 - Geometry 1	4.39	5.15	0.74
1 - Geometry 2	4.06	5.51	1.2
2 - Geometry 1	3.61	3.89	0.77
2 - Geometry 2	3.34	4.17	1.22
3 - Geometry 1	9.79	10.03	0.66
3 - Geometry 2	9.44	11.46	0.81
4 - Geometry 1	6.76	6.79	0.58
4 - Geometry 2	6.63	7.70	0.79
5 - Geometry 1	3.59	3.50	0.67
5 - Geometry 2	3.23	3.65	0.87

the exit velocity is less than for the baseline configuration to maintain the same mass flow rate. Thus the lower static pressure drop can be misleading, while the total pressure drop takes all the important variables into account.

As shown Table (4.3) the total pressure drop of the increased outflow configuration is consistently greater than that of the baseline configuration. Thus the impact of increasing the outlet area on the pressure drop was detrimental for all conditions tested. The increase in pressure drop for these five runs ranged from 4% at the lower

mass flow rate and high pressures and temperatures of Run 5 to 14% for the high mass flow rate of the third run.

4.2.4 Temperature Pattern and Profile. The temperature pattern is very important at combustor exits. Table (4.3) shows the comparison between pattern factors for the baseline and increased outflow area configurations. As in the pressure drop comparison, the increased outflow area UCC does quite poorly in runs 1 and 2 where the pressure and mass flow are relatively low. For the higher pressure (runs 3, 4, and 5) it does significantly better, however the baseline configuration still has a more uniform outflow temperature. We can also visually see how the outflows of the original and increased outflow area configurations compare by looking at Figures (4.1) and (4.8).

Figure (4.8) shows the temperature contours looking out from the outlet of the increased outflow area configuration. This can be compared with the temperature contours of the baseline configuration as shown in Figure (4.1). This, as well as the temperature pattern calculations shown in Table (4.3), show the baseline configuration with a much more uniform temperature pattern at the exit.

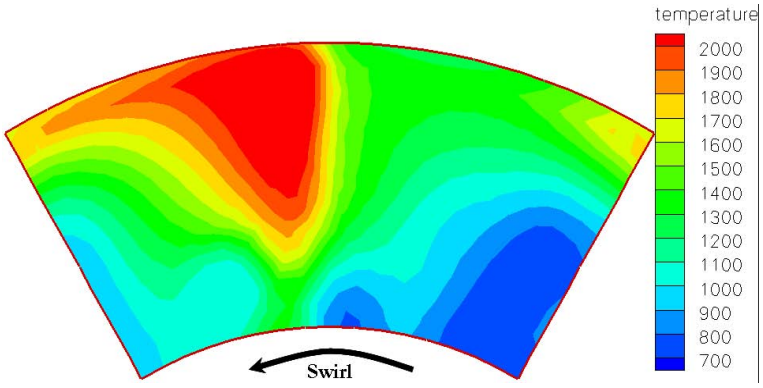

Figure 4.8: Run 1 Temperature Contours at Outlet of Increased Outflow Area (Geometry 2)

Figures (4.2) and (4.9) show the temperature contours at various planes through the combustor for the baseline and increased outflow area configurations. The temperature distribution is more uniformly distributed throughout the cavity in the baseline

configuration than in the increased outflow area configuration. In neither case however are the high temperatures clustered on the cavity wall. This is another essential characteristic in the combustor where the material life can be severely limited by high temperature areas on the surfaces. This better temperature distribution of the baseline configuration remains true as the flow leaves the cavity and flows toward the outlet. On the increased outflow configuration, the high temperatures are clustered to the vane and the outflow distribution remains very uneven. This is shown in Figure (4.9) and Table (4.3).

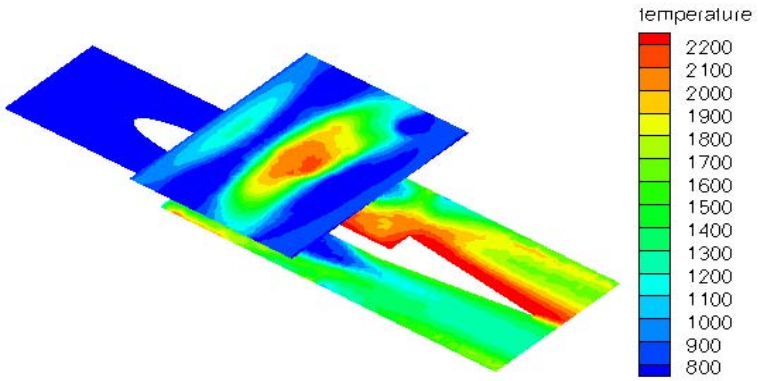

Figure 4.9: Run 1 Cutaway Temperature Contours of Increased Outflow Area (Geometry 2)

4.3 Impact of Decreased Cavity Jet Velocity

The second comparison between the numerical geometry configurations was made by doubling the diameter of the cavity air inlet jets while maintaining the mass flow rate constant. This has the effect of decreasing the velocity of the air through the cavity jets by 400% and decreasing the overall angular momentum in the cavity. CFD analysis showed that the maximum circumferential velocities were decreased by about 250% in the decreased cavity jet velocity configuration. A comparison of this cavity velocity can be seen in velocity contour plots of the various configurations as shown in Appendix A.

This was done in an effort to simulate the effects of cases where it may be possible to maintain the mass flow rate to the cavity, however the pressure required

Table 4.4: Baseline(Geometry 1) vs Decreased Cavity Jet Velocity Configuration(Geometry 3) Emission and Efficiency Comparison

Run	CO(ppm)	CO_2(%)	O_2(%)	NO_x(ppm)	HC(ppm)	η(%)
1 - Geometry 1	997	5.2	12.8	64.4	100	96.0
1 - Geometry 3	997	4.9	13.2	114	196	94.1
2 - Geometry 1	1016	5.1	12.8	59.0	124	95.2
2 - Geometry 3	909	4.9	13.1	112.6	208	94.1
3 - Geometry 1	454	2.6	16.8	18.1	66	95.2
3 - Geometry 3	511	2.4	17.2	22.1	98	93.2
4 - Geometry 1	424	3.0	16.2	19.9	70	95.7
4 - Geometry 3	535	2.8	16.5	29.4	120	93.0
5 - Geometry 1	1334	5.8	11.8	88.5	84	96.6
5 - Geometry 3	1103	5.6	12.0	112.5	192	94.1

for an increased velocity may not be possible. The results of this study are outlined below and shown in Tables (4.4) and (4.5).

4.3.1 Efficiency and Emissions Impact. Sturgess et al. [26] found that low cavity air jet momentum led to poorly organized air flow in the cavity and thus decreased efficiency. As is generally the case at high pressures, the combustion efficiency of the combustor tends to be limited mainly by the mixing rate. [14]

As shown in Table (4.4), the CO is not significantly altered due to the decreased cavity circumferential velocity, however, both the NO_x and unburned hydrocarbons show considerable increases. The NO_x and HC increase by an average of about 53 and 82%, respectively. This is evidence of the importance of mixing in the UCC. As the cavity air jets are decreased in velocity, the mixing is significantly decreased which results in an efficiency decreased by an average of over two percent from the baseline for these five runs. Therefore, it is important to maintain sufficient cavity air velocity in the UCC in order to maintain combustor efficiency.

4.3.2 Cavity Velocity Profiles. Figure (4.10) shows the velocity vectors of the flow through the cavity in the decreased cavity velocity configuration contour colored by temperature. The difference between this flow profile and that of the

baseline configuration (see Figure (4.3) is quite dramatic. It becomes very apparent in this case that the combustion is not occurring very well within the cavity. This is most likely due to the decreased mixing capability of this configuration and accounts for the large amounts of unburned hydrocarbons exiting the combustor.

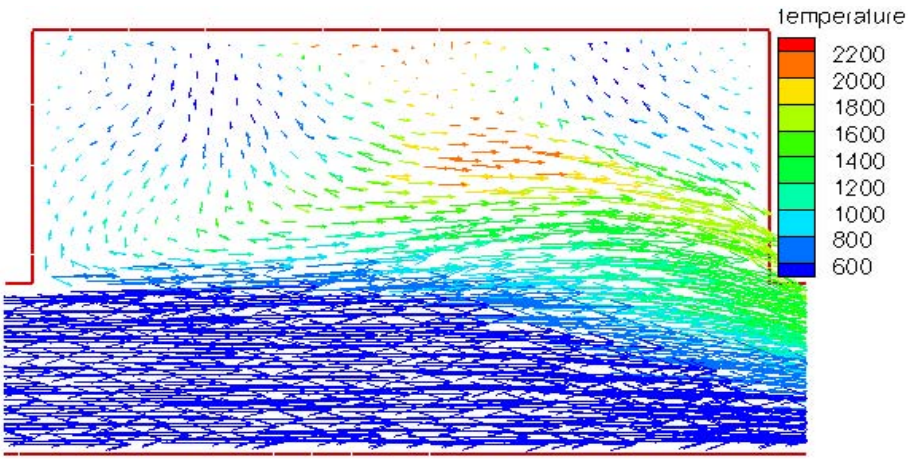

Figure 4.10: Cavity Velocity Vectors (Colored by Temperature Contours) of Decreased Cavity Jet Velocity (Geometry 3) on Periodic Boundary (Run 1)

The distinct stratification between the hot and cold regions as show in Figure (4.3) are not as clear on Figure (4.10). This is another big indication that the circumferential velocities are insufficient to create the centrifugal forces necessary to throw the heavier, cold species out to the cavity wall while allowing the hotter, combustion products to move to the center to join the main airflow.

4.3.3 Pressure Loss Comparison. The decreased cavity circumferential velocity had only a slight impact on the pressure drop over the combustor. The numerical results support the idea that the high circumferential velocities in the cavity have little impact on the overall pressure drop over the combustor. In fact, in this case the higher circumferential velocity resulted in slightly lower pressure losses. This could be of great interest for future design work to know that the pressure drop is not a limiting factor in cavity circumferential velocities.

Table 4.5: Baseline(Geometry 1) vs Decreased Cavity Jet Velocity Configuration(Geometry 3) Pressure Loss and Pattern Factor Comparison

Run	$\frac{dP}{P}_{abs}$ (%)	$\frac{dP}{P}_{total}$ (%)	Pattern Factor
1 - Geometry 1	4.39	5.15	0.74
1 - Geometry 3	4.53	5.28	0.71
2 - Geometry 1	3.61	3.89	0.77
2 - Geometry 3	3.77	4.00	0.71
3 - Geometry 1	9.79	10.03	0.66
3 - Geometry 3	10.18	10.22	0.85
4 - Geometry 1	6.75	6.79	0.58
4 - Geometry 3	6.94	6.84	0.79
5 - Geometry 1	3.59	3.50	0.67
5 - Geometry 3	3.86	3.78	0.68

4.3.4 Temperature Pattern and Profile. Figure (4.11) shows the temperature contours on the outlet plane for the decreased cavity velocity configuration. The pattern is comparable to that of the baseline configuration as shown in Table (4.5). However, as can be seen by comparing Figures (4.11) and (4.1), the profiles of the two configurations are quite different. As stated early, the desired temperature profile is one in which the temperature remains constant for a given radius with a maximum temperature slightly above the mean radius value. While neither configuration has an optimal profile, the baseline configuration is clearly closer to the ideal.

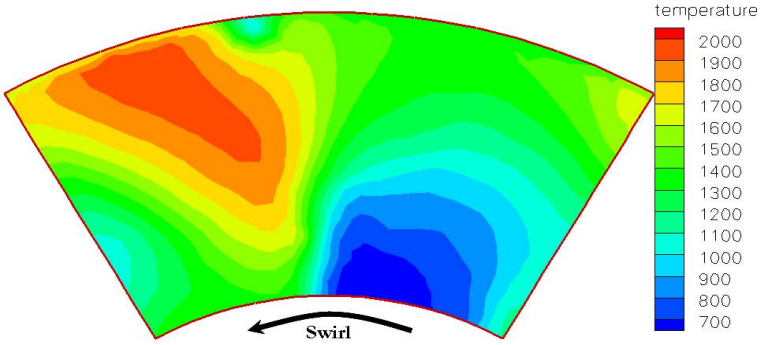

Figure 4.11: Run 1 Temperature Contours at Outlet of Decreased Cavity Jet Velocity (Geometry 3)

The cavity temperature contour in the decreased cavity velocity configuration is not well distributed thoughout the cavity. It is beneficial to have walls that are

shielded from the extreme high temperatures as is the case here as shown in Figure (4.12). The velocity vectors in Figure (4.10) show even further how the high temperature region is a small area in the center of the cavity. In a better mixed combustion process the high temperatures would likely be more uniform throughout the cavity.

As shown in Figure (4.12), this configuration also uses the vane as a type of flameholder with the combustion happening on the opposite side of the cavity swirl hitting the vane. This concentration of high temperatures on one side of the vane is the reason for the poor temperature profile exhibited by this configuration.

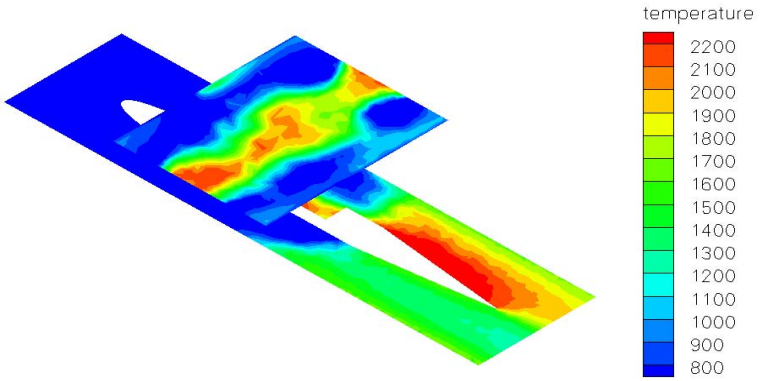

Figure 4.12: Run 1 Cutaway Temperature Contours of Decreased Cavity Jet Velocity (Geometry 3)

4.4 Impact of Decreased Cavity Length

The fourth comparison was made to determine the effect of decreasing the cavity length. It was postulated that the cavity size of the original UCC configuration is more than sufficient and that decreasing the cavity length could actually increase the efficiency of the combustor, decrease the combustor weight, and increase the fuel-air mixing in the cavity. Initial CFD analysis such as the velocity vectors colored by temperature shown in Figure (4.3) appeared to support this idea.

The cavity length was decreased by removing $\frac{3}{16}th$ inch off each end of the cavity ring, leaving the fuel injector and cavity air jets in the same configuration with respect

to one another. It should be noted that this modification puts the cavity air jets closer to the front and rear flanges. However, the cavity air jet distance to the flanges was determined to be sufficiently far as to not result in significant friction drag directly on the air jets.

4.4.1 Efficiency and Emissions Impact. On average, the NO_x, CO, and HC emissions as shown in Table (4.4) are all slightly increased for the decreased cavity length configuration. However, these differences are small and result in no more than a one percent decrease in combustor efficiency. It is also important to look at the individual operating conditions for the cases to determine where the decreased cavity length configuration performs the best in comparison with the original configuration.

As can be seen in Table (4.4), the decreased cavity length configuration performs the best in Run 3 which has a total mass flow rate of nearly 78 $\frac{lb}{min}$ and an inlet pressure and temperature of 59K and 530 degrees Fahrenheit, respectively. In this case the decreased cavity length configuration has an efficiency 0.3% higher than the baseline configuration and has lower HC and CO emissions. It is noteworthy that this run has the highest operating mass flow rate and temperature tested with the pressure just 3 psia below the maximum. This indicates that as the temperature and pressures continue to increase, the decreased cavity length may continue to perform as efficiently or more efficiently than the baseline configuration.

4.4.2 Cavity Velocity Profiles. Figure (4.13) shows the velocity vectors of the flow through the cavity in the decreased cavity length configuration colored by temperature. It is of interest to note that the high temperature area of this configuration and of the baseline configuration are very similarly shaped and sized. This seems to indicate that the baseline configuration did have an unused area which could be removed. It also appears quite possible that the cavity length could be decreased even further with minimal impact.

Table 4.6: Baseline(Geometry 1) vs Decreased Cavity Length Configuration(Geometry 4) Emission and Efficiency Comparison

Run	CO(ppm)	CO_2(%)	O_2(%)	NO_x(ppm)	HC(ppm)	η(%)
1 - Geometry 1	997	5.2	12.8	64.4	100	96.0
1 - Geometry 4	1204	4.9	13.1	88.4	122	95.1
2 - Geometry 1	1016	5.1	12.8	59.0	124	95.2
2 - Geometry 4	1198	4.91	13.1	85.7	120	95.1
3 - Geometry 1	454	2.6	16.8	18.1	66	95.2
3 - Geometry 4	437	2.3	17.3	20.3	61	95.5
4 - Geometry 1	424	3.0	16.2	19.9	70	95.7
4 - Geometry 4	446	2.9	16.4	25.7	79	95.3
5 - Geometry 1	1334	5.8	11.8	88.5	84	96.6
5 - Geometry 4	1684	5.5	12.2	91.4	109	95.6

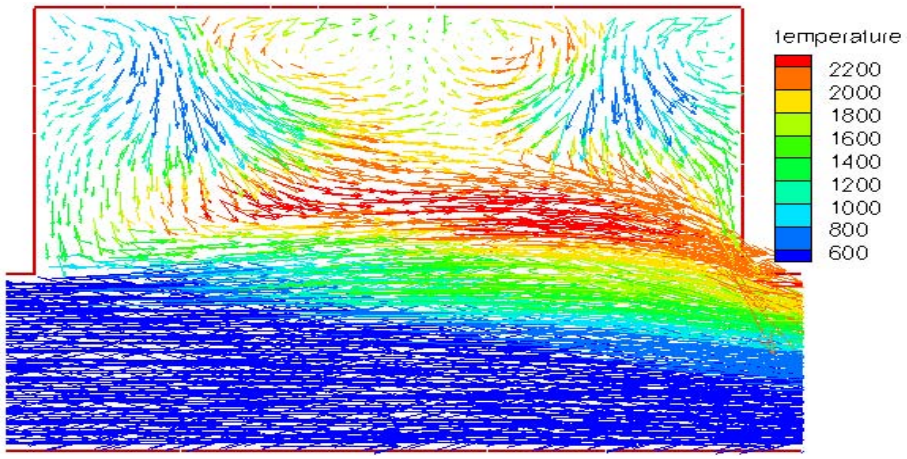

Figure 4.13: Cavity Velocity Vectors of Decreased Cavity Length (Geometry 4) on Periodic Boundary (Run 1)

The distinct stratification between the hot and cold regions as show in Figure (4.13) for the decreased cavity length configuration are even more pronounced than those of the baseline configuration shown on Figure (4.3). It also appears to be much flatter than the baseline configuration. This is perhaps indicative of a better designed cavity where the colder fuel and air are centripetally accelerated to the cavity wall, and can only return to the main flow by combusting into less dense reactants.

4.4.3 Pressure Loss Comparison. The velocity contours as shown in Figure (4.13) may also help explain why the decreased cavity length configuration shows

Table 4.7: Baseline(Geometry 1) vs Decreased Cavity Length Configuration(Geometry 4) Pressure Loss and Pattern Factor Comparison

Run	$\frac{dP}{P}_{abs}$ (%)	$\frac{dP}{P}_{total}$ (%)	Pattern Factor
1 - Geometry 1	4.39	5.15	0.74
1 - Geometry 4	4.08	4.83	1.0
2 - Geometry 1	3.61	3.89	0.77
2 - Geometry 4	3.40	3.68	1.0
3 - Geometry 1	9.79	10.03	0.66
3 - Geometry 4	8.65	9.00	0.94
4 - Geometry 1	6.75	6.79	0.58
4 - Geometry 4	6.25	6.28	0.84
5 - Geometry 1	3.59	3.50	0.67
5 - Geometry 4	3.40	3.36	0.91

a clear decrease (0.2 to 1%) in both static and total pressure drops over the baseline configuration. As was noted, the higher temperature region is much flatter in the decreased cavity length configuration indicating that perhaps the cavity flow is better contained. This, along with the mixing length (equal to the cavity length), is quite likely the reason for the lower pressure drop.

As was the case with the emissions and efficiency, the decreased cavity length configuration performed the best under the highest temperature and mass flow rate conditions. The pressure for this run (Run 3), at 59 degrees, was also only 3 psia less than the maximum inlet pressure. This is very important considering that actual flight conditions are generally higher in pressure and temperature than was modeled here. This configuration also has significantly lower pressure loss than both the increased outflow area and decreased cavity velocity configurations.

4.4.4 Temperature Pattern and Profile. The cavity temperature contours for the decreased cavity length design as shown in Figure (4.15) are well designed with the extreme temperatures distributed fairly evenly within the cavity and away from the walls. However, as the flow exits the cavity the temperature uniformity is not as well distributed as the high temperature area remains close to the vane on the side shielded from the high swirl flow. The possibility that the vane is acting as a flame

stabilizer in the main flow is evident. This is not a desired distribution and it remains to be seen if a vane design modification would provide a more uniform outflow.

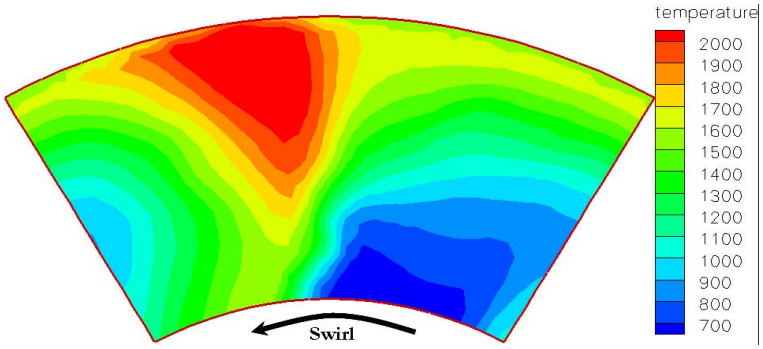

Figure 4.14: Run 1 Temperature Contours at Outlet of Decreased Cavity Length (Geometry 4)

This flow pattern non-uniformity is further emphasized by the high pattern factor values as shown in Table (4.7) which were all approximately 25 percent higher than for the original configuration. The temperature contours, shown as looking out from the combustor, in Figure (4.14) give a visual image of how the temperature is distributed at the outlet. It should also be noted that the profile, or radial distribution, of the temperature is better in the original configuration.

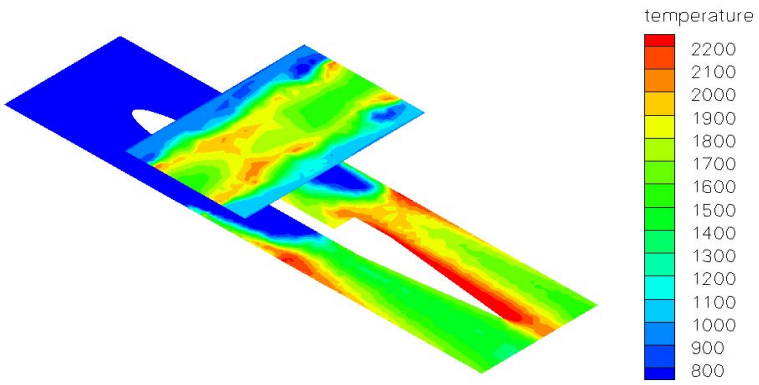

Figure 4.15: Run 1 Cutaway Temperature Contours of Decreased Cavity Length (Geometry 4)

4.5 Impact of Vane Curvature

The final comparison was made to determine the effect of adding curvature to the axially oriented vane. As has been discussed previously, the flow pattern and profile at the exit plane are not optimal and it is likely that the vane configuration in these designs may be part of the problem. The final design of the UCC is intended to consist of a curved vane, serving as the turbine inlet turning vane. The exact specifications of this configuration have not yet been determined, nor built for experimental test. However, as an initial step towards understanding the impact vane curvature would have on the flow patterns, and possibly even the engine efficiency, a numerical model was constructed with a 0.2 radian curvature.

The decreased cavity length configuration was used as the initial starting point with the only modification being the addition of the 0.2 radians of curvature in the direction of the swirl introduced by the cavity jets.

4.5.1 Efficiency and Emissions Impact. Because the curved vane design was based on the decreased cavity length configuration, all comparisons were made with that configuration rather than the baseline. The emissions and efficiency results are included in Table (4.8). The CO for each run is increased with the curved vane configuration. The first four show CO increases between 15 and 34%. The final run, which is a high pressure (61 psia), high temperature (526^oF), and low mass flow rate ($37\ \frac{lbm}{min}$) shows a considerable CO increase of 75%.

As discussed earlier, CO production is an integral part of the combustion process. However, most CO produced reacts with the oxygen to form CO_2. This is a rapid reaction as long as the temperature is sufficiently high and the residence time is sufficiently long. If these two parameters are not met, the CO can become frozen in the flow and becomes a pollutant. The curved vane configuration curves with the flow through the combustor. This is likely decreasing the residence time in the combustor and allowing the CO to exit unreacted. This would indicate that for increased residence time and decreased CO emissions, the curvature of the vane should be at much

Table 4.8: Decreased Cavity Length Configuration(Geometry 4) vs Decreased Cavity Length with Curved Vane Configuration(Geometry 5) Emission and Efficiency Comparison

Run	CO(ppm)	CO_2(%)	O_2(%)	NO_x(ppm)	HC(ppm)	η(%)
1 - Geometry 4	1204	4.9	13.1	88.4	122	95.1
1 - Geometry 5	1614	4.9	13.2	67.2	110	95.0
2 - Geometry 4	1198	4.9	13.1	85.7	120	95.1
2 - Geometry 5	1542	4.8	13.2	64.7	107	95.1
3 - Geometry 4	437	2.3	17.3	20.3	61	95.5
3 - Geometry 5	504	2.2	17.4	16.5	64	95.2
4 - Geometry 4	446	2.9	16.4	25.7	79	95.3
4 - Geometry 5	541	2.9	16.3	30.5	73	95.4
5 - Geometry 4	1684	5.5	12.2	91.4	109	95.6
5 - Geometry 5	2955	5.3	12.3	67.5	101	94.6

greater. This increased curvature would also likely increase mixing and combustion in the outflow volume.

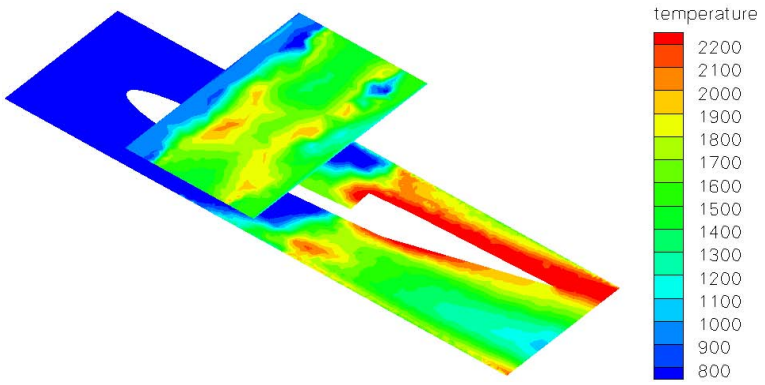

Figure 4.16: Run 1 Cutaway Temperature Contours of Decreased Cavity Length with Curved Vane (Geometry 5)

The decrease in residence time could also partly explain the decrease in NO_x of the curved vane configuration. The parameters that affect the formation of NO_x are primarily temperature and residence time, although the former is generally more significant. For each case, with the exception of the Run 3, the decrease in NO_x for the curved vane configuration was between 8 to 12%. This may be related to the decrease in residence time in the combustor. It is also possible that the high temperature regions were more spread out due to the vane curvature. This appears

to be supported by a comparison of Figures (4.15) and (4.16) which show the curved vane with combustion on both sides, appearing to increase the combustion area in the outflow.

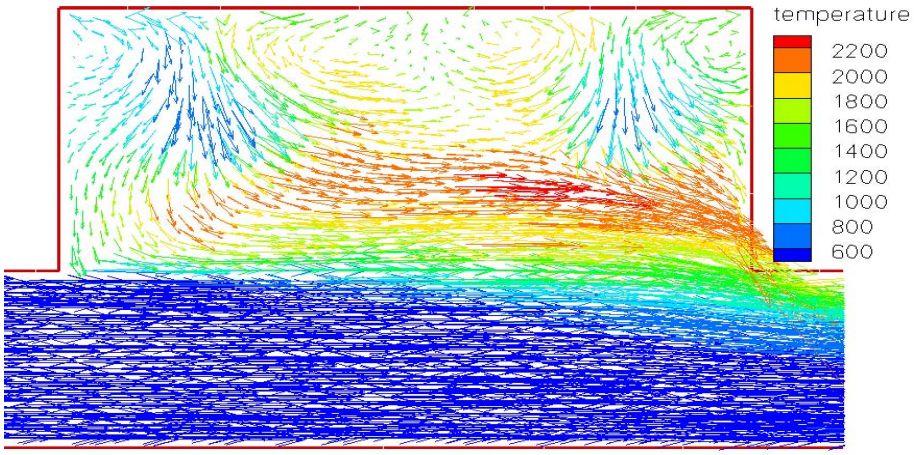

Figure 4.17: Cavity Velocity Vectors of Decreased Cavity Length with Curved Vane (Geometry 5) on Periodic Boundary

4.5.2 Cavity Velocity Profiles. Figure (4.17) shows the velocity vectors of the flow through the cavity in the decreased cavity length with curved vane configuration colored by temperature. The flow and temperature patterns of this in comparison with the decreased cavity length configuration as shown in Figure (4.13) are very similar. If anything, it appears that the curved vane may cause the high temperature area to be slightly more stretched out in the cavity, with the flame being more contained within the cavity.

4.5.3 Pressure Loss Comparison. Table (4.9) shows the static and total pressures for the decreased cavity length with curved (Geometry 5) and uncurved vanes (Geometry 4). The pressured drop varies only very slightly between for the curved vane configuration which shows about 0.1% decrease in total pressure drop. This decrease is likely due to the better alignment of the vane curvature with the exiting flow. The variation between operating conditions was minimal for the pressure drop with the mass flow rate seeming to be the most important criteria. For the low

Table 4.9: Decreased Cavity Length Configuration(Geometry 4) vs Decreased Cavity Length with Curved Vane Configuration(Geometry 5) Pressure Loss and Pattern Factor Comparison

Run	$\frac{dP}{P}_{abs}$ (%)	$\frac{dP}{P}_{total}$ (%)	Pattern Factor
1 - Geometry 4	4.08	4.83	1.0
1 - Geometry 5	4.11	4.76	1.17
2 - Geometry 4	3.40	3.68	1.0
2 - Geometry 5	3.42	3.62	1.16
3 - Geometry 4	8.65	9.00	0.94
3 - Geometry 5	8.82	8.89	0.85
4 - Geometry 4	6.25	6.28	0.84
4 - Geometry 5	6.26	6.14	1.06
5 - Geometry 4	3.40	3.36	0.91
5 - Geometry 5	3.39	3.28	1.05

total mass flow rate conditions, Runs 1 (35.5 $\frac{lbm}{min}$), 2 (35.9 $\frac{lbm}{min}$), and 5 (37.4 $\frac{lbm}{min}$) the decrease in pressure drop is about 0.7% while the higher mass flow rate conditions of Runs 3 (77.7 $\frac{lbm}{min}$) and 4 (62.8 $\frac{lbm}{min}$) show larger pressure drop decreases greater than 0.11%.

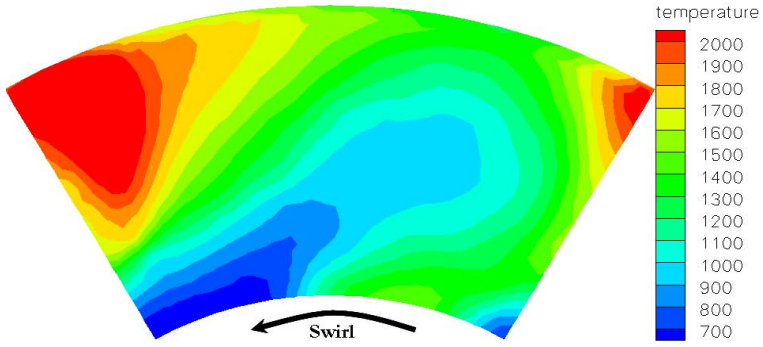

Figure 4.18: Run 1 Temperature Contours at Outlet of Decreased Cavity Length with Curved Vane (Geometry 5)

4.5.4 Temperature Pattern and Profile. The cavity temperature contours for the curved vane design as shown in Figure (4.16) are very similar to that of the decreased cavity length design as shown in Figure (4.15). However, the outflow region shows significant differences. In the curved vane configuration, the high temperature regions are on both sides of the vane as opposed to just the one side. This is due to the

swirl added to the flow by the cavity. In the decreased cavity length configuration, the combustion is occuring on the opposite side of the swirl hitting the vane. However, in the curved vane design, the combustion is occuring on both sides of the vane due to the aligment of the vane with the flow. These high temperatures on the vane surfaces could cause problems in the UCC and ways to get the flame more uniform in the outflow region need to be addressed.

The pattern factors at the outlet for the curved vane configuration as given in Table (4.9) indicate that the non-uniformity of temperature in the flow continues to the outlet. Figure (4.18) visually shows the temperature contours as looking out from the combustor. It is possible that increasing the curvature would help alleviate this non-uniformity but this is a topic of future study.

4.6 Design Impact Summary

	CO	NOx	UHC	Efficiency	Pressure Drop
Increased Outflow Area	++	++	++	--	++
Decreased Cavity Velocity	±	++	++	--	±
Decreased Cavity Length	±	+	±	±	--
Curved Vane	++	±	±	±	--

Very Undesirable Effect
Undesirable Effect
Minimal Effect
Very Desirable Effect
Desirable Effect
Minimal Effect

Figure 4.19: Configuration Trends as compared with the Baseline Configuration

A qualitative summary of the impacts that the configuration changes had on the UCC performance is shown in Figure (4.19). From this it can be seen that the

Table 4.10: Mean Droplet Injection Diameters Test Conditions

Injector	Cone Angle (deg)	Variation from Mean Diameter	Percent Fuel Flow
1	80	-15 microns	10
2	60	-5 microns	25
3	70	0	30
4	64	+5 microns	25
5	76	+15 microns	10

increased outflow area and decreased cavity velocity configurations both had undesirable effects on the UCC performance. The decreased cavity length configurations showed considerable improvement in the pressure drop with minimal impact on the combustor efficiency.

4.7 Fuel Droplet Size Comparison

In order to better understand the relation between the fuel droplet size and the combustor efficiency, several runs were made on the baseline configuration (Geometry 1) with various fuel mean droplet sizes at injection. Tests varied from mean droplet diameters, D_{mean}, of 45 to 85 microns with droplet distributions, injection cone angles, and percent fuel flow rates as indicated in Table (4.10). In order to indroduce this droplet distribution into Fluent it was necessary to use five cones with the same injection position. In this manner the five injection cones overlayed each other providing a droplet size distribution and spray pattern more closely resembling that of experimental tests.

As the fuel droplet mean diameter increases, the residence time require for complete burning is greatly increased. Therefore, the percentage of unburned hydrocarbons leaving the combustor is increased which results in a significant loss in engine efficiency. An understanding of the droplet diameter where the residence time becomes insufficient to completely combust the fuel is important in the design process to ensure an efficient combustion process.

Table 4.11: Results of Increased Mean Droplet Injection Diameters

D_{mean}(microns)	$\frac{dP}{P}(\%)$	CO(ppm)	$CO_2(\%)$	$O_2(\%)$	$C_{12}H_{23}$(ppm)	$\eta_b(\%)$
45	4.3	1663	5.7	11.9	33.5	97.1
50	4.3	1336	5.5	12.2	59.2	96.8
55	4.4	1033	5.2	12.8	100.2	96.0
65	4.3	621	4.5	13.9	179.7	94.2
75	3.8	380	3.5	15.4	449.7	86.4
85	3.3	335	2.6	16.9	736.2	77.9

The results of increasing the mean droplet diameter are shown in Table (4.11). As the droplet diameter increases, the combustion becomes less efficient as more unburned hydrocarbons exit the combustor. This leaves the O_2 unreacted and at higher concentrations, the CO_2 and CO levels are both significantly lower due to the lack of combustion, and the efficiency drops off drastically.

All droplet mean diameter tests were run at the conditions for case 1: pressure = 41.7 psig, temperature = 530 K, $\dot{m}_{main} = 29\ \frac{lb}{min}$, $\dot{m}_{cavity} = 6.4\ \frac{lbm}{min}$, Cavity ϕ = 1.62, Overall $\phi = 0.294$, and fuel flow = 42.4 $\frac{lb}{hr}$.

4.8 Cavity in a Cavity

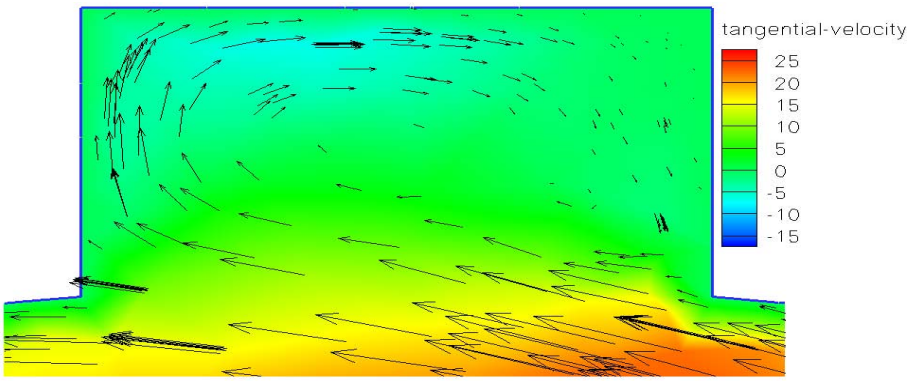

Figure 4.20: Cavity in a Cavity Velocity Contours

The small axially oriented cavity on the outer wall of the main cavity is known as the Cavity in a Cavity (CIAC). It is into this axial cavity that the fuel is injected and is an effort to shield the fuel spray from the high circumferential velocities. This

CIAC design has shown to be effective at stabilizing the flame in experimental tests. Figure (4.20) shows the velocity contours of a cross section of the small axially-oriented cavity into which the fuel is injected. The velocity vectors superimposed on the contour plot show how the injected fuel is initially shielded from the high speed circumferential flow of the main cavity. It also appears that the main cavity circumferential velocities shed some of the flow into the CIAC in the form of a trapped vortex.

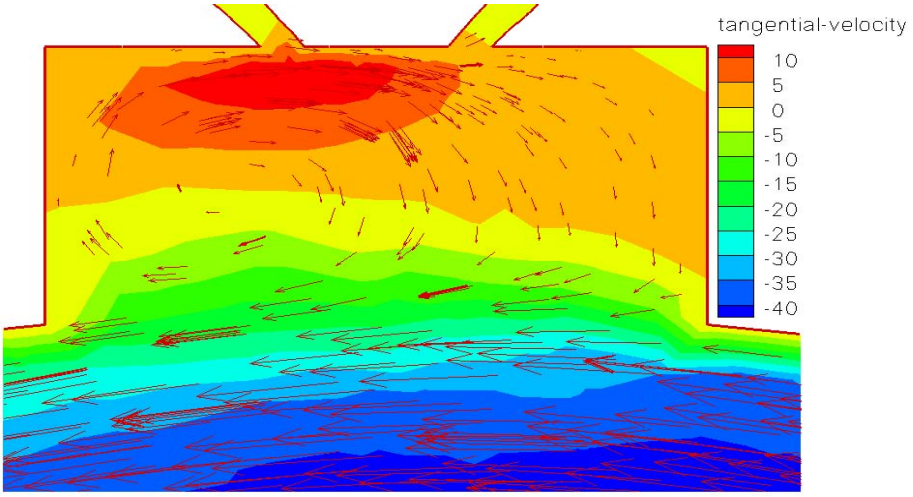

Figure 4.21: Cavity in a Cavity Velocity Contours (in plane with injector)

Figure (4.21) is the same cross-sectional view of the axial cavity but it is in the plane of the fuel injector. Once again, the velocities inside the cavity are greatly reduced from the high circumferential velocities of the main cavity flow and a trapped vortex appears inside of the small axial cavity (CIAC).

4.9 Total Pressure Drop Comparison

A comparison of the total pressure drop vs air mass flow rate between the various configurations is shown in Figure (4.22). As the mass flow rate increases the pressure drop over the combustor for each configuration also increases.

The increased outflow area configuration has the highest pressure drop for each case. It is noteworthy however, that for the lower air mass flow rates the difference is

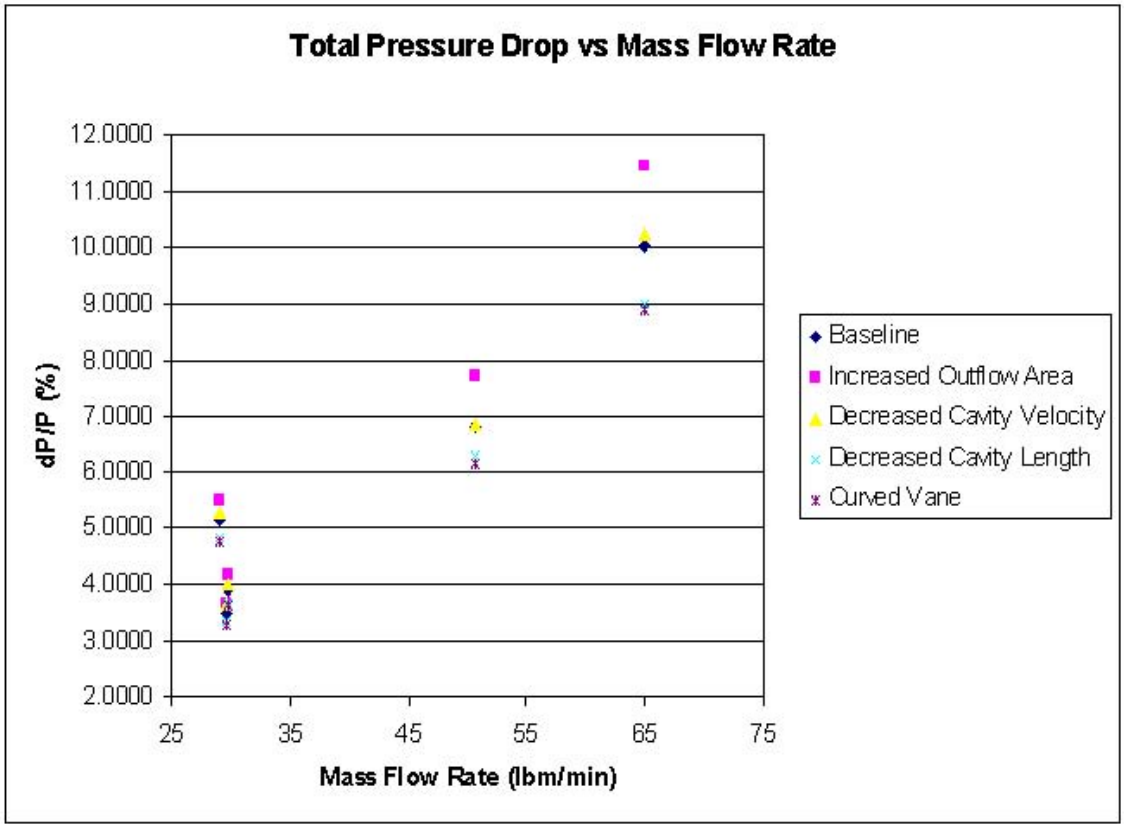

Figure 4.22: Total Pressure Drop vs Mass Flow Rate for all Numerical UCC Geometries.

much smaller than for the higher air mass flow rate conditions. As the mass flow rate increases, the difference in pressure drop becomes much greater between the increased outflow and the other configurations.

The original and decreased cavity velocity configurations had similar pressure drops. This is indication that the cavity circumferential velocity has little impact on the overall pressure drop of the combustor.

The decreased cavity length showed large decreases in pressure drop in both the curved and straight vane configurations. As the air mass flow rate is increased, the decrease in pressure drop from the baseline configuration also increases from a 4 to 6% decrease at the lower mass flow rates to a 10% decrease at the highest mass flow rate.

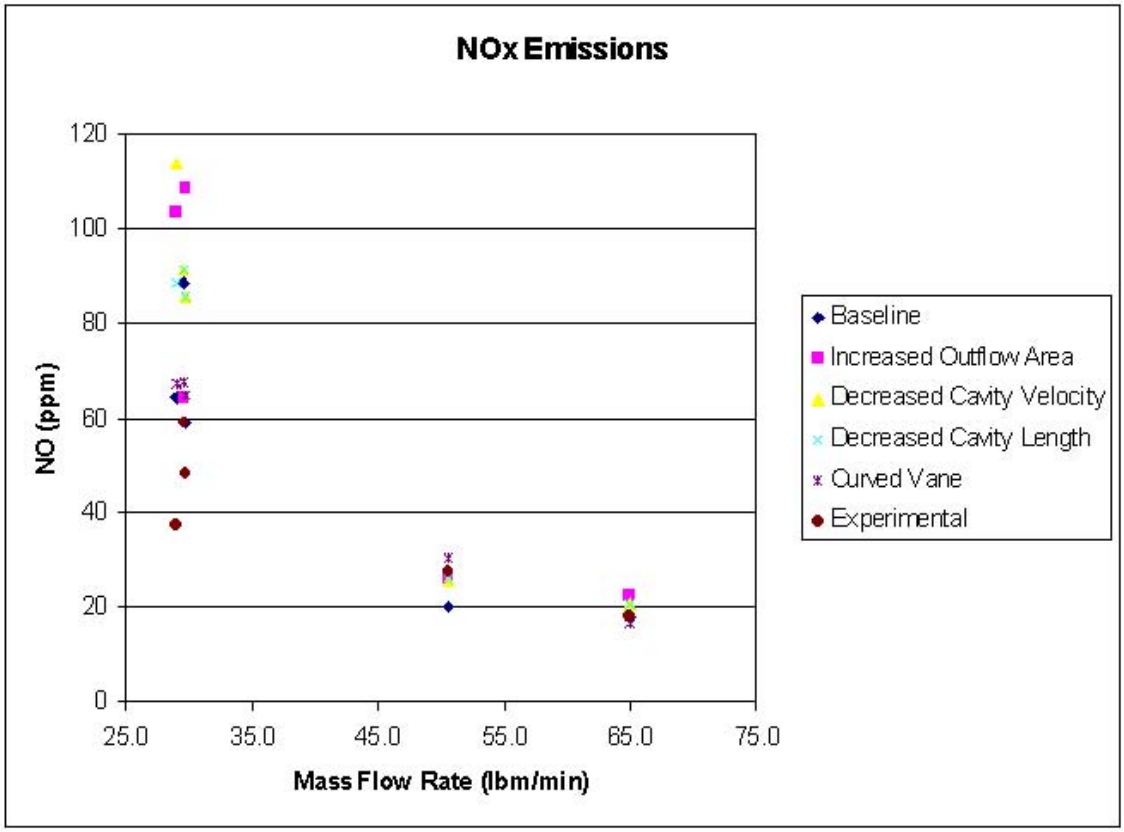

Figure 4.23: NO_x vs Mass Air Flow.

Figures 4.23 and 4.24 show how carbon monoxide CO and NO_x emissions, respectively, trend for the different UCC numerical configurations as well as the experimental data. These figures are another validation that the numerical model is doing what is necessary in this case, which is to show trends of increased or decreased performance. For all combustor configurations, the decreased mass flow rate results in an increase in pollutant emissions. The increased outflow and decreased cavity velocity configurations have consistently higher emissions than the original and decreased cavity length configurations although the difference is diminished in the higher mass flow rate cases.

As the mass flow rate increases, the amount of expelled unburned hydrocarbons also decreases as depicted in Figure (4.25). However, when the variations of fuel flow

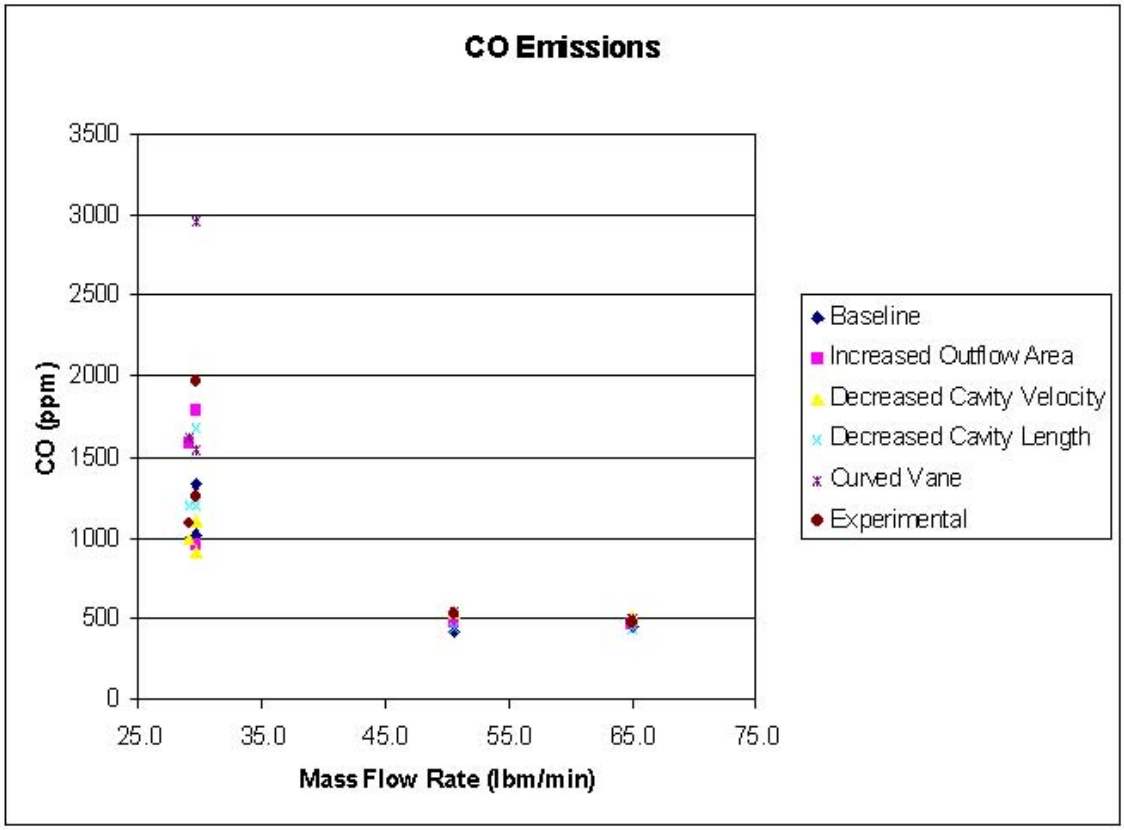

Figure 4.24: CO vs Mass Air Flow.

are taken into account as in Figure (4.26), the amount of pollutant per kilogram of fuel actually tends to increase. This fuel flow variation is taken into account in the calculation of the Emission Index (EI) as defined in Equation (1.2) where it can be seen that each physical UCC configuration has an emission index range of less than 20 points.

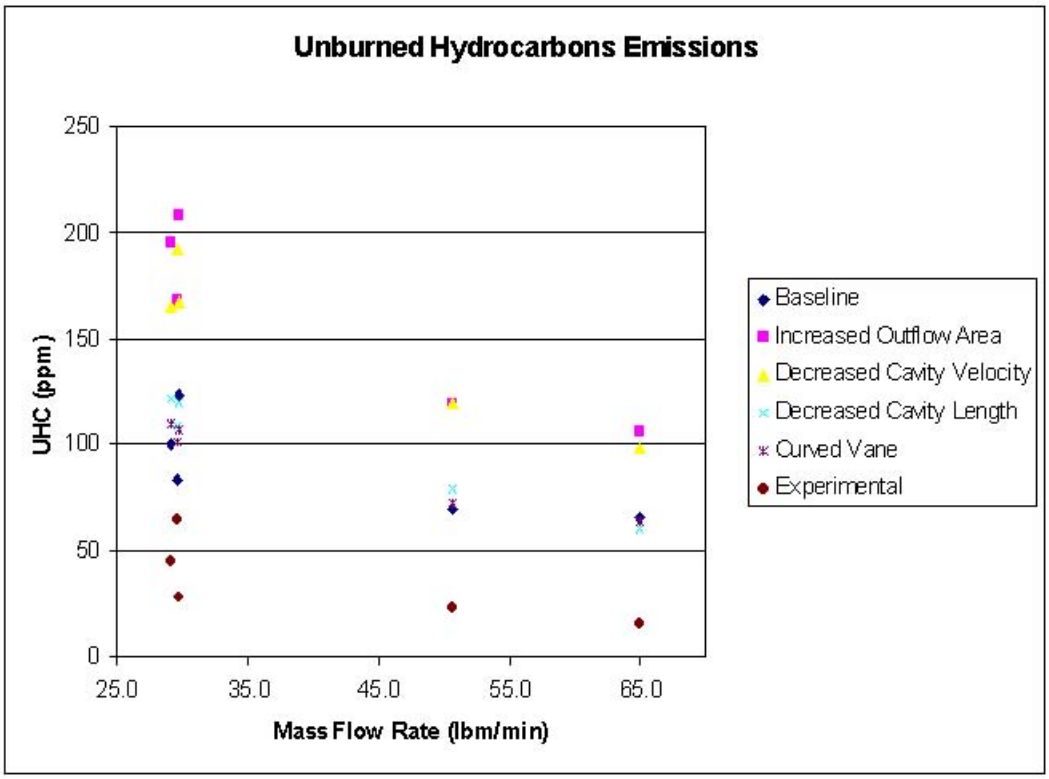

Figure 4.25: Unburned Hydrocarbons vs Mass Air Flow

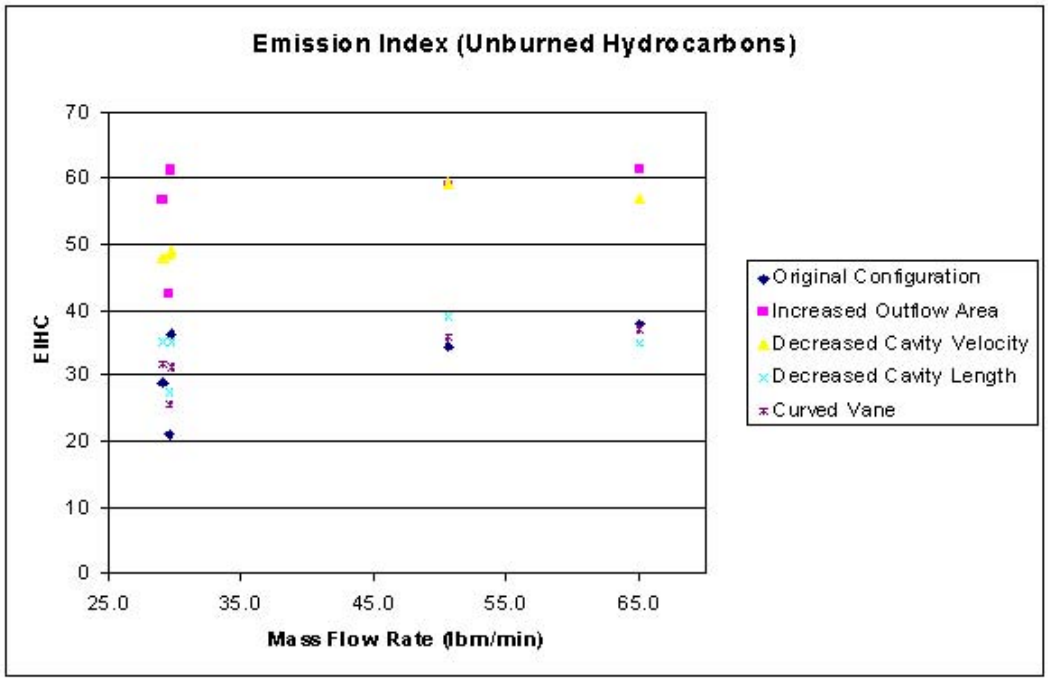

Figure 4.26: Emissions Index of Unburned Hydrocarbons vs Mass Air Flow.

V. Conclusion

A numerical analysis of four configurations of the Ultra Compact Combustor, Cavity-in-a-Cavity design has been conducted and compared with experimental results. A commercial Computational Fluid Dynamics (CFD) package was used throughout the process to model the flow and combustion process through the combustor. The CFD results compared favorably with the experimental results over a wide range of inlet pressures and temperatures, as well as pressure drops and equivalence ratios.

Besides the current UCC configuration which was tested experimentally, four other configurations were modeled numerically to determine the effect the design changes would have on the UCC efficiency, emissions, pressure drop, and temperature patterns. These four alternative configurations were an increased outflow area, a decreased cavity jet velocity, a decreased cavity length, and a decreased cavity length and curved vane combination. Each variant, except for the curved vane configuration, was compared to the current UCC design and evaluated.

It was determined that the 26 percent increase in the outflow area has the effect of slightly increasing the total pressure loss and the pattern factor through the combustor in all the operating conditions run. The increased outflow area also results in lower combustor efficiency in the lower pressure cases. However, as the pressure is increased, it is more comparable to the original configuration in regards to efficiency and emissions - especially as the mass flow rate is reduced. This design shows promise when operating at the high pressures. Continued optimization of the design may show that a certain degree of increased outflow area is beneficial to the UCC design, but this is the subject of further research.

The decreased cavity air jet velocity performs reasonably well for the cases run. It has a pressure drop comparable to the original configuration and a fairly uniform temperature pattern on the outlet. However, the decreased mixing due to the decreased circumferential velocity is very evident when the pollutant emissions are included. High circumferential velocities are imperative in order to get the increased flame speeds as shown in the centrifugal enhanced bouyancy studies by Lewis [16].

It is recommended that in cases where the circumferential velocities required of the UCC cannot be maintained, that other configurations should be considered.

The decreased cavity velocity configuration showed also that the cavity circumferential velocity had little impact on overall pressure drop. This may be of considerable importance in future design work indicating that the cavity velocities need to be reduced for pressure drop considerations.

The decreased cavity length shows a increase in pollutant emissions, except in the highest temperature and mass flow rate flow where the combustor efficiency exceeds that of the original configuration. This is significant because future operating conditions of the UCC will be higher than those temperatures and pressures tested. Also, the pressure loss over this configuration is significantly less (at least 4 to 10%) than any of the other configurations and shows great potential with a further optimization of the vane and other parameters. One clear advantage this configuration has over the others is the decreased weight due to the decrease in volume. All else being equal, a lighter combustor would always be the most desireable.

The curved vane configuration shows a increase in CO emissions and a decrease in NO_x and unburned hydrocarbons over the decreased cavity length configuration. This is likely due in part to the decreased residence time in the combustor due to the alignment of the vane with the flow. The pressure loss over this configuration is also slightly (0.1%) less than the decreased cavity length design. The velocity profile over the exit plane was made much more uniform due to the vane curvature, however, the temperature pattern and profile were made worse. The curvature implemented in this design was very small and it remains to be seen if an increase in the curvature will produce a more desireable temperature pattern at the exit by increasing the mixing in the main flow area.

From analysis of the outflow velocities and temperatures of each of the UCC configurations, one readily apparent commonality is the poor flow uniformity. As flow enters the turbine, flow nonuniformity causes temperature hot spots and a rythmic

beating on the turbine blades as they go from one flow temperature and velocity to another. This significantly decreases the MTBM of the turbine.

It appears that much of the reason for this lack of temperature and velocity uniformity is the lack of axial curvature in the vanes. The eventual plan for these axially oriented vanes is to make them curved vanes serving as the first stage turbine turning vanes. From analysis of the outflow characteristics it appears that the insertion of curved vanes would very likely result in a substantial increase in flow uniformity at the exit. As the cavity flow enters the main airflow through the combustor a significant bit of swirl is added to the flow. It is believed that a vane with axial curvature would turn with this swirling flow and likely not create the large non-uniformities at the exit plane. The curved vane configuration was an initial step in understanding this flow uniformity. In these conditions, the temperature pattern became worse with the curved vane. However, by increasing the curvature above what was tested in this configuration, may better distribute the high temperatures at the exit plane and needs to be tested.

Another related observation can be seen in Figures (4.9), (4.12), and (4.15). In each of these temperature contour plots it can be seen that the vane is serving as a flame holder. These high temperatures attached to the vane would require either cooling of the vane or a lowering of the combustor average temperature in order to maintain a respectable MTBM. It also seems very likely that the opposite side of the vane is not subject to these same temperatures due to the impact of the swirling flow as it leaves the cavity. This appears to be validated by the curved vane design which shows combustion occuring on both sides of the vane due to its alignment with the flow. The temperature contours of the curved vane configuration are shown in Figure (4.16).

The Cavity in a Cavity design has effectively enhanced the flame stability and increased the blow out velocities in experimental tests. The numerical analysis of the cross-sectional velocities within the cavity further show how the CIAC is effective.

It is recommended that this be maintained as an integral part of the UCC design. However, optimization of the actual CIAC dimensions may increase its functionality even further and should be conducted as the UCC continues to evolve.

5.1 Future Work

The effect of several different physical configuration parameters are not yet completely optimized. For example, the optimal placement of the cavity air jets with respect to the fuel injector and/or the walls is an important parameter that must be better understood to enhance the fuel-air mixing in the combustor.

Analysis of vane curvature is one significant area that should be researched. One obvious shortcoming of the current system is the flow non-uniformity at the exit plane. It would be very advantageous to conduct a numerical study of several different vanes with varying curvature, culminating in a design which would more uniformly distribute the flow patterns and conserve the natural swirl momentum created in the cavity as it leaves the combustor and enters the turbine. Once this numerical study is complete, experimental tests could be conducted to verify the design.

Further optimization of the CIAC dimensions to best maintain the trapped vortex characteristics. Also, fuel injection angles into the cavity could be conducted.

Time-resolved solutions of the flow field would shed further light on the UCC flow patterns and characteristics.

Cavity length reduction appeared to bring desireable results, especially in pressure losses through the combustor. Various other lengths could be tested numerically to determine an optimal cavity length.

Outflow area had a negative impact in the cases studied. Further studies to determine if there is an optimal outflow/inflow area ratio where the pressure drop is minimized and the combustor efficiency is maximized could be conducted.

Higher pressure and temperature conditions can be tested numerically much easier than experimentally and should be done as a precursor to future planned higher pressure and temperature experiments.

Experimental analysis and verification of the numerical results attained herein should be conducted on the decreased cavity length configuration.

Appendix A

Velocity Contours of Various UCC Configurations

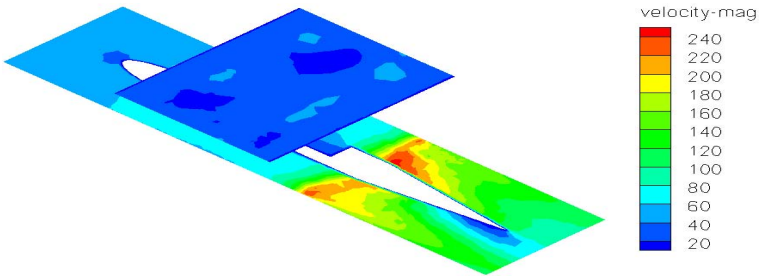

Figure 0.1: Run 1 Cutaway Velocity Contours of Experimental Configuration (Geometry 1)

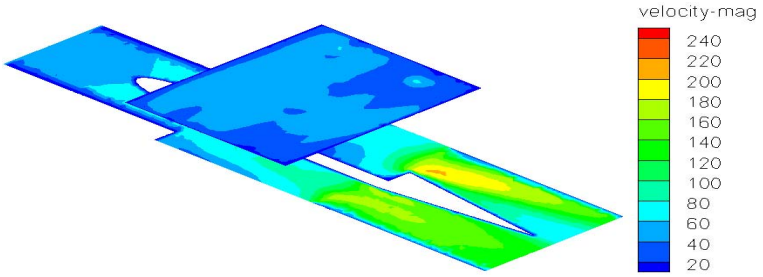

Figure 0.2: Run 1 Cutaway Velocity Contours of Increased Outflow Area (Geometry 2)

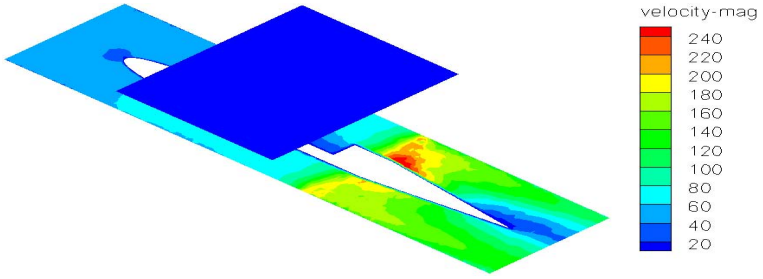

Figure 0.3: Run 1 Cutaway Velocity Contours of Decreased Cavity Jet Velocity (Geometry 3)

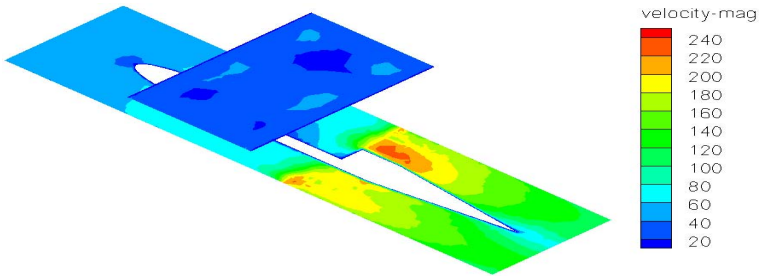

Figure 0.4: Run 1 Cutaway Velocity Contours of Decreased Cavity Length (Geometry 4)

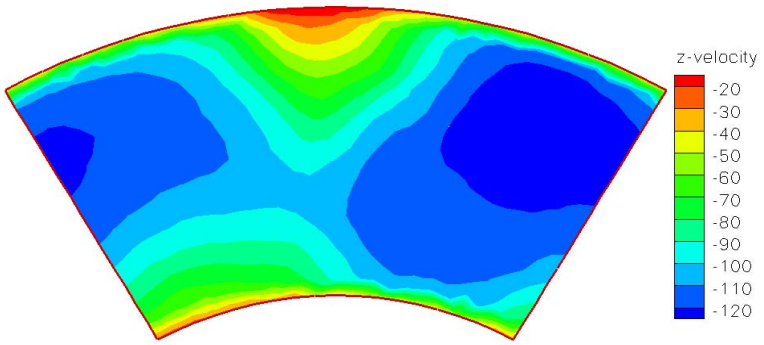

Figure 0.5: Run 1 Outlet Velocity Contours of Decreased Cavity Length (Geometry 4)

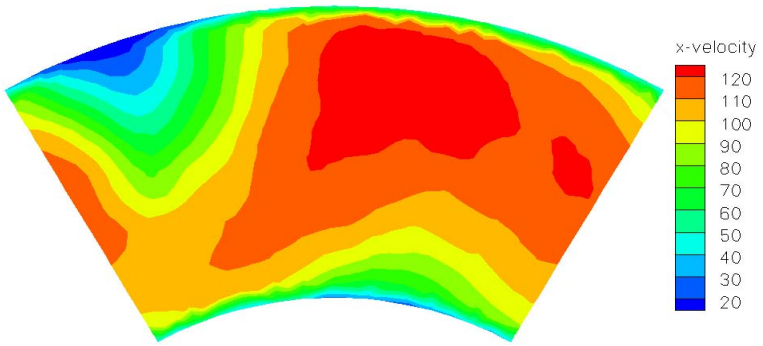

Figure 0.6: Run 1 Outlet Velocity Contours of Decreased Cavity Length with Curved Vane (Geometry 5)

Appendix B

Velocity Vectors for Experimental Configuration

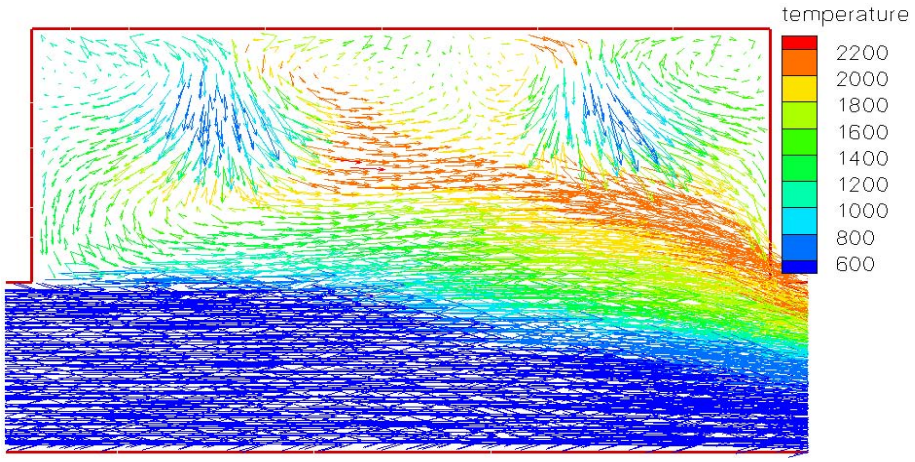

Figure 0.7: Cavity Velocity Vectors of Experimental Configuration (Geometry 1) on Periodic Boundary (Run 2)

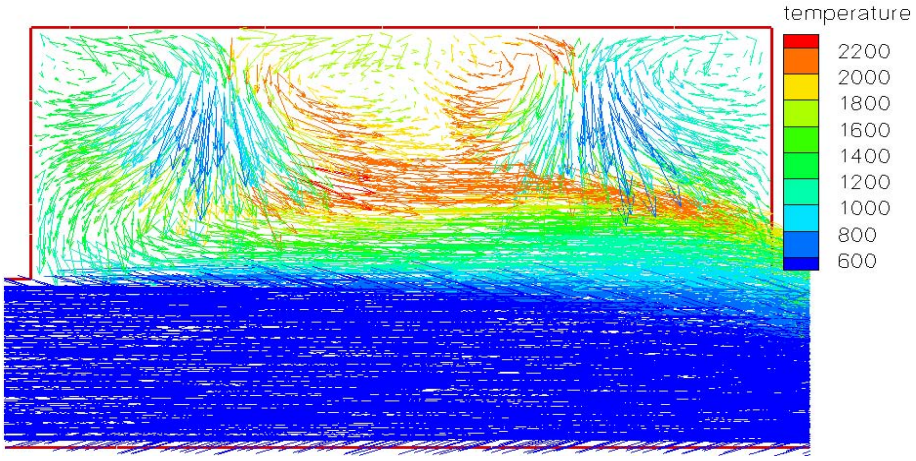

Figure 0.8: Cavity Velocity Vectors of Experimental Configuration (Geometry 1) on Periodic Boundary (Run 3)

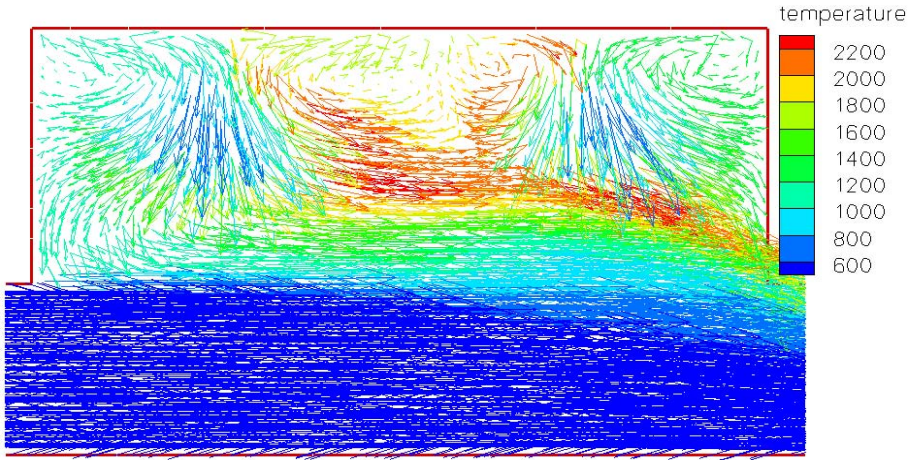

Figure 0.9: Cavity Velocity Vectors of Experimental Configuration (Geometry 1) on Periodic Boundary (Run 4)

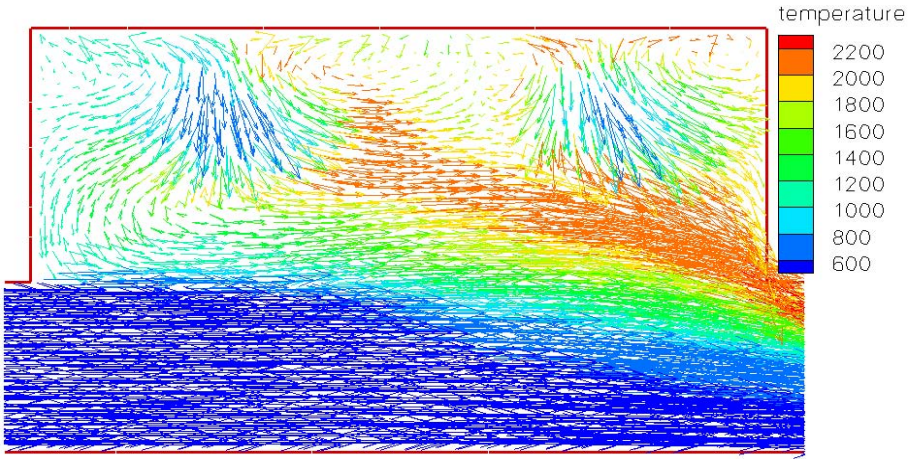

Figure 0.10: Cavity Velocity Vectors of Experimental Configuration (Geometry 1) on Periodic Boundary (Run 5)

Appendix C

Velocity Vectors for Increased Outlet Area Configuration

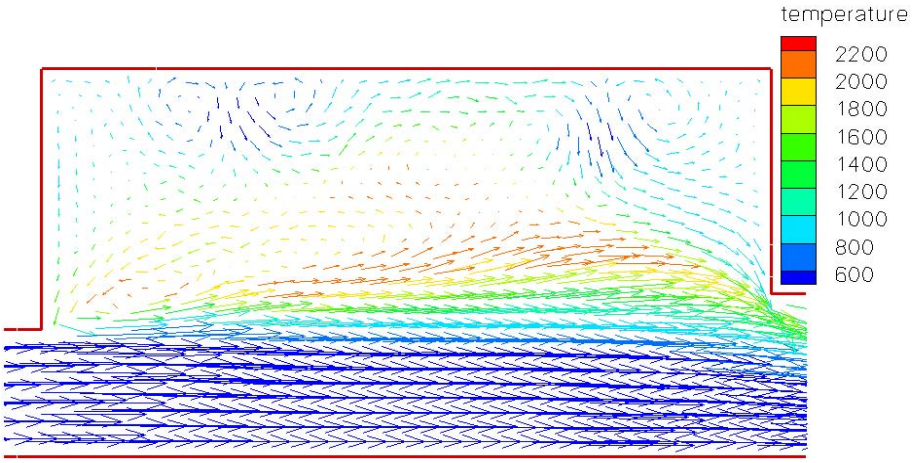

Figure 0.11: Cavity Velocity Vectors of Increased Outflow Area Configuration (Geometry 2) on Periodic Boundary (Run 2)

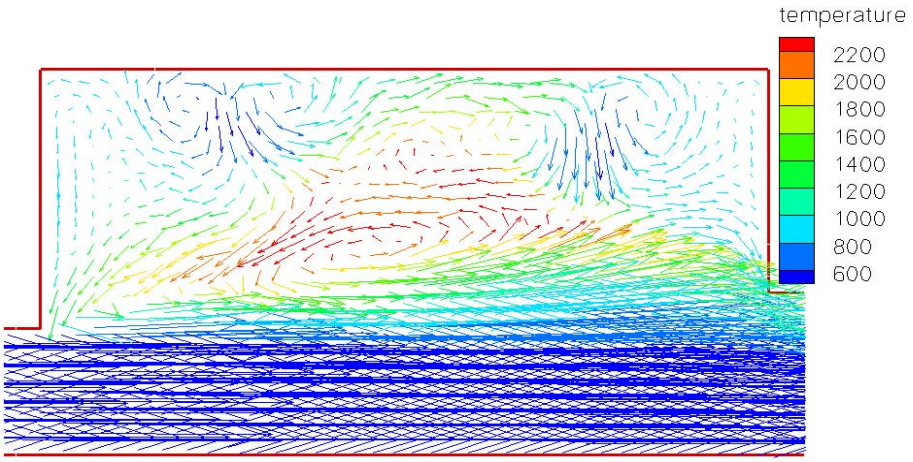

Figure 0.12: Cavity Velocity Vectors of Increased Outflow Area Configuration (Geometry 2) on Periodic Boundary (Run 3)

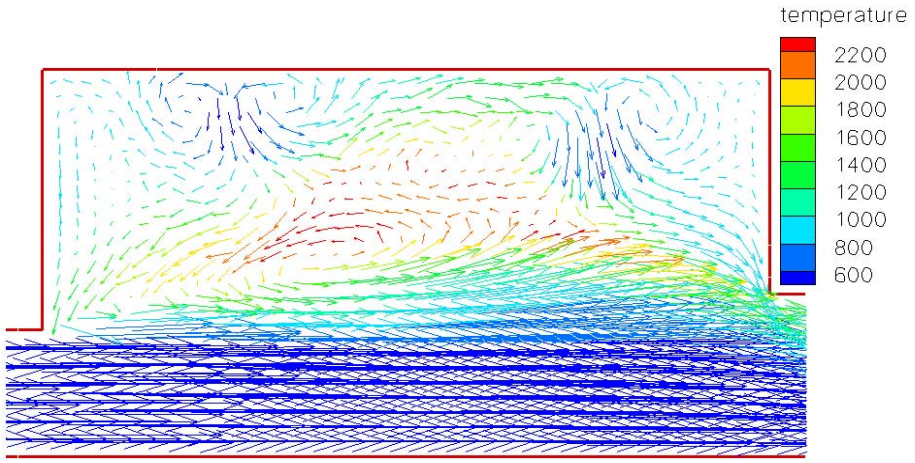

Figure 0.13: Cavity Velocity Vectors of Increased Outflow Area Configuration (Geometry 2) on Periodic Boundary (Run 4)

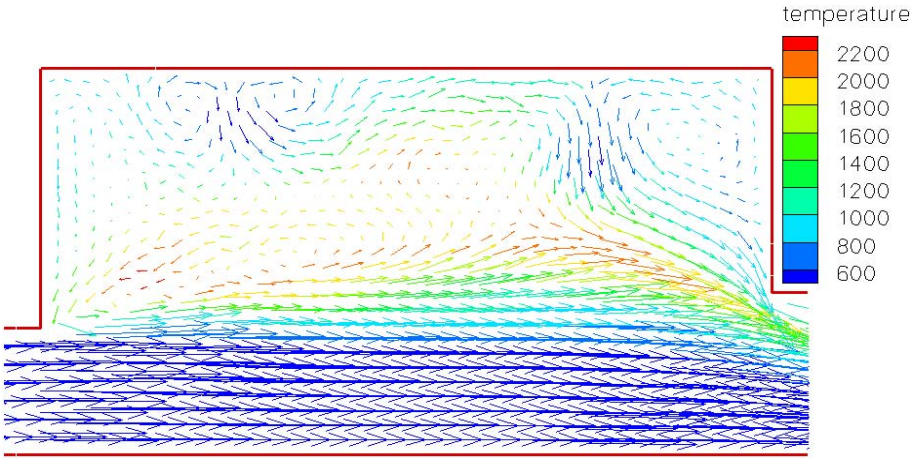

Figure 0.14: Cavity Velocity Vectors of Increased Outflow Area Configuration (Geometry 2) on Periodic Boundary (Run 5)

Appendix D

Velocity Vectors for Decreased Cavity Velocity Configuration

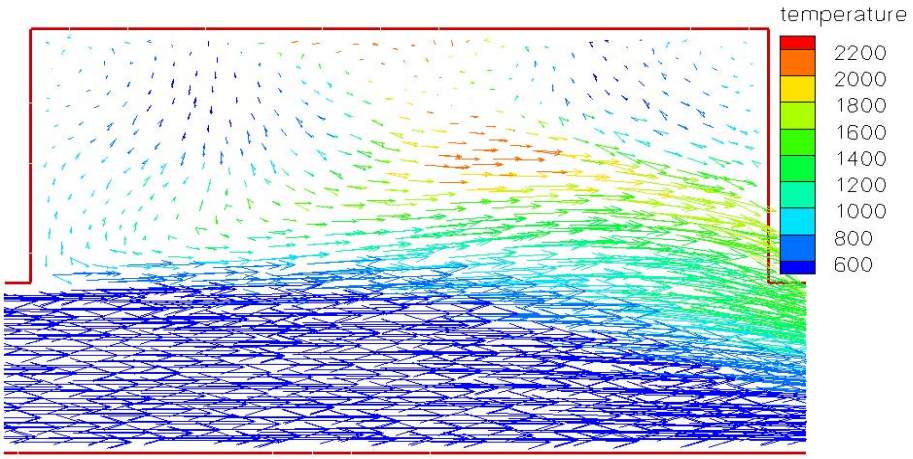

Figure 0.15: Cavity Velocity Vectors of Decreased Cavity Velocity Configuration (Geometry 3) on Periodic Boundary (Run 2)

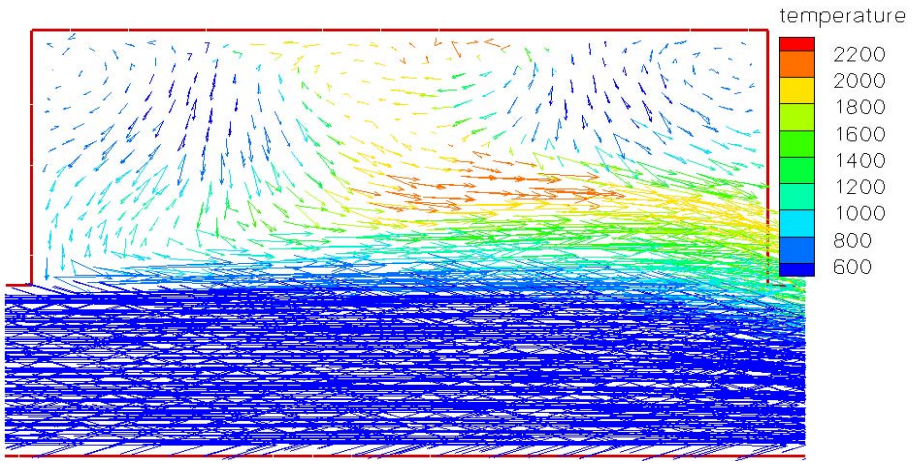

Figure 0.16: Cavity Velocity Vectors of Decreased Cavity Velocity Configuration (Geometry 3) on Periodic Boundary (Run 3)

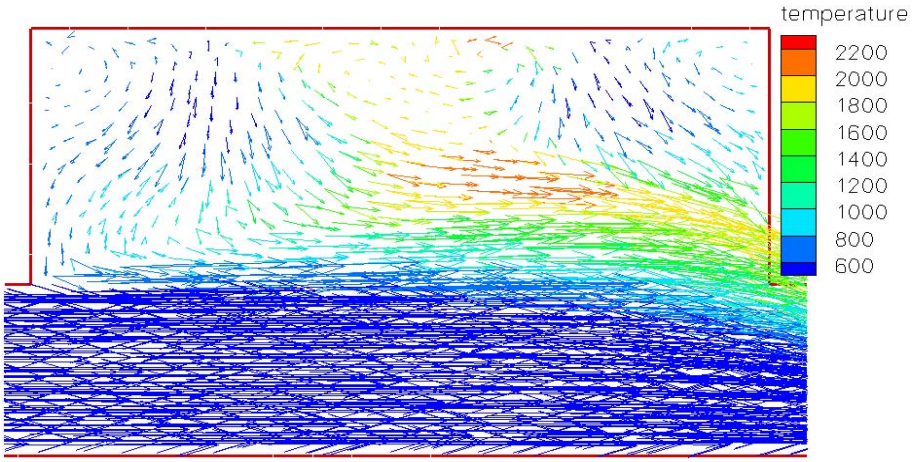

Figure 0.17: Cavity Velocity Vectors of Decreased Cavity Velocity Configuration (Geometry 3) on Periodic Boundary (Run 4)

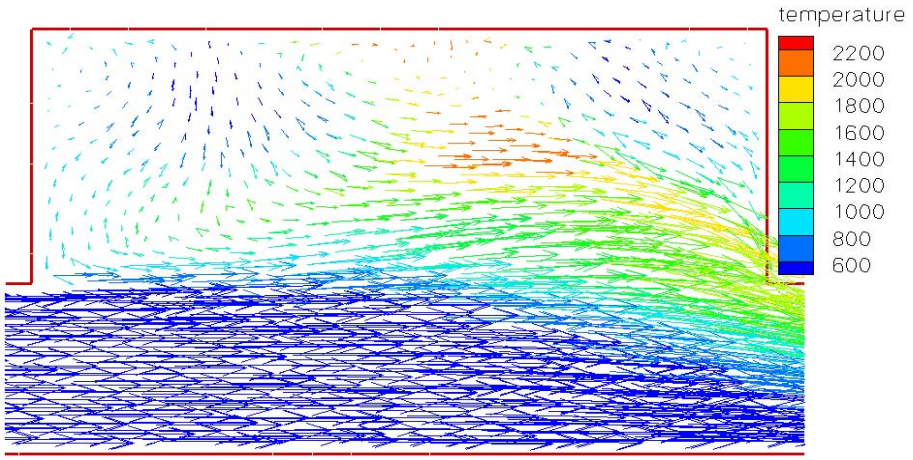

Figure 0.18: Cavity Velocity Vectors of Decreased Cavity Velocity Configuration (Geometry 3) on Periodic Boundary (Run 5)

Appendix E

Velocity Vectors for Decreased Cavity Length Configuration

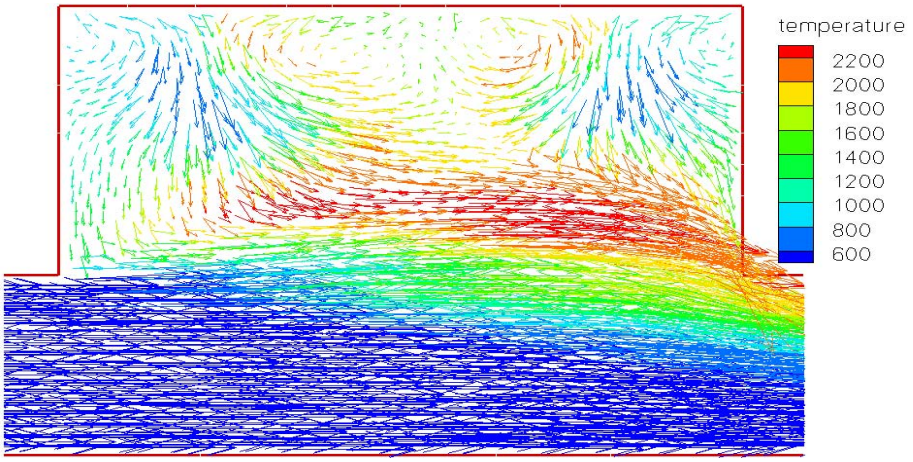

Figure 0.19: Cavity Velocity Vectors of Decreased Cavity Length Configuration (Geometry 4) on Periodic Boundary (Run 2)

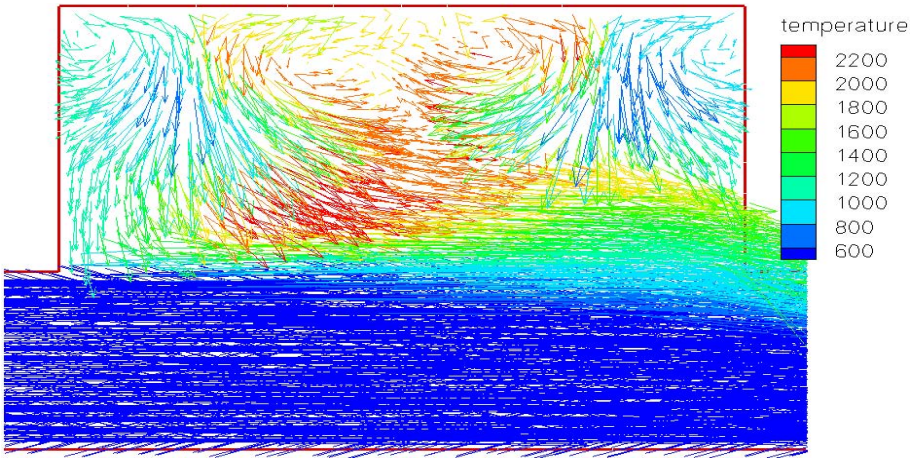

Figure 0.20: Cavity Velocity Vectors of Decreased Cavity Length Configuration (Geometry 4) on Periodic Boundary (Run 3)

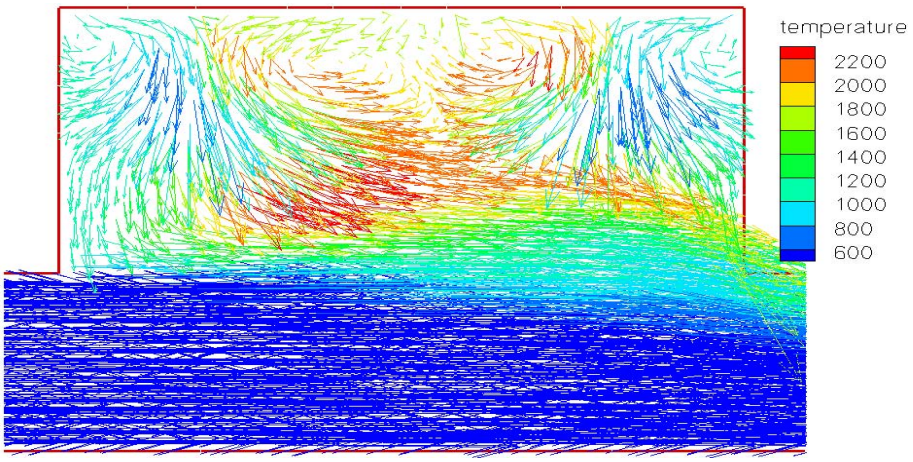

Figure 0.21: Cavity Velocity Vectors of Decreased Cavity Length Configuration (Geometry 4) on Periodic Boundary (Run 4)

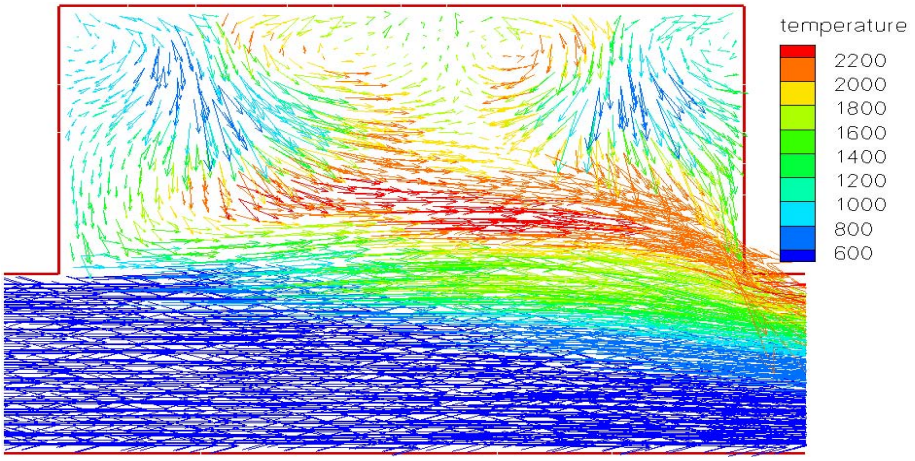

Figure 0.22: Cavity Velocity Vectors of Decreased Cavity Length Configuration (Geometry 4) on Periodic Boundary (Run 5)

Appendix F

Velocity Vectors for Decreased Cavity Length with Curved Vane

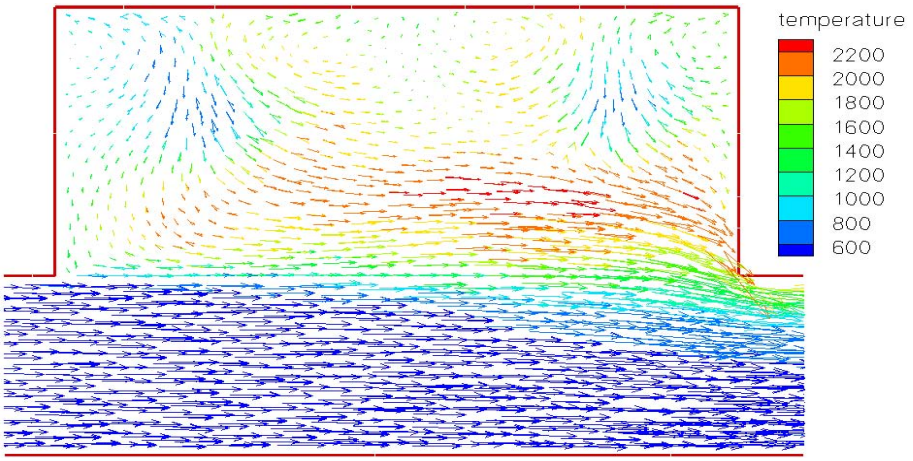

Figure 0.23: Cavity Velocity Vectors of Decreased Cavity Length with Curved Vane (Geometry 5) on Periodic Boundary (Run 2)

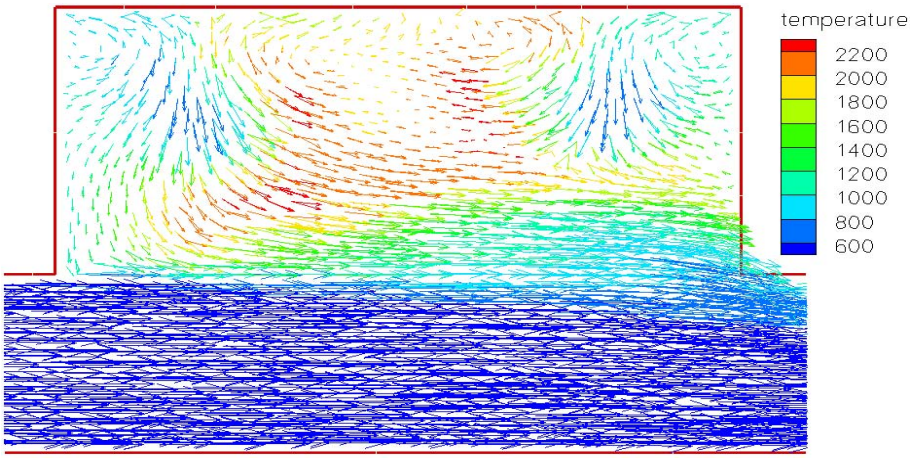

Figure 0.24: Cavity Velocity Vectors of Decreased Cavity Length with Curved Vane (Geometry 5) on Periodic Boundary (Run 3)

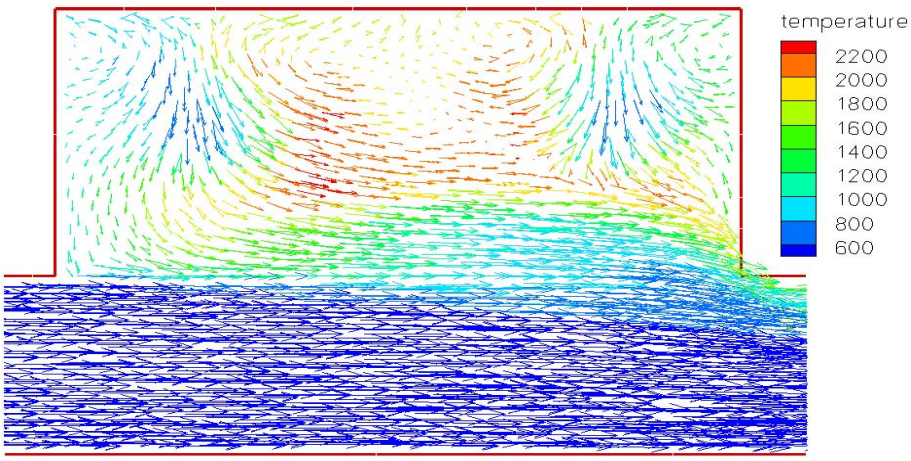

Figure 0.25: Cavity Velocity Vectors of Decreased Cavity Length with Curved Vane (Geometry 5) on Periodic Boundary (Run 4)

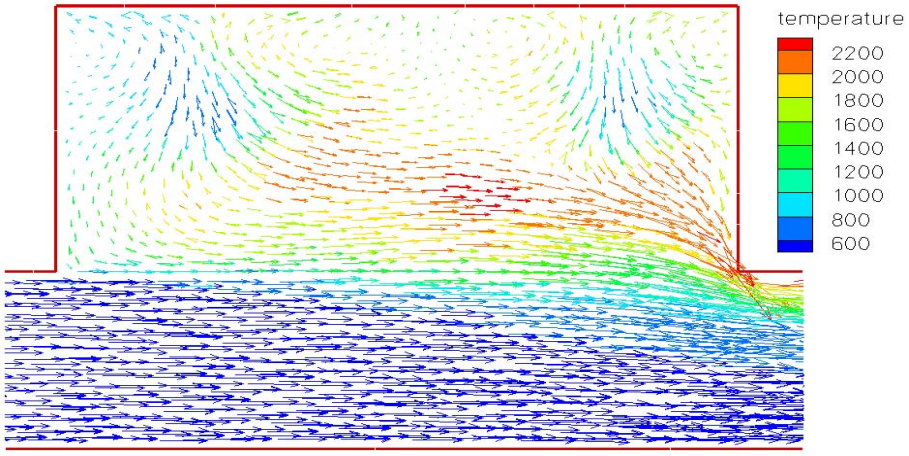

Figure 0.26: Cavity Velocity Vectors of Decreased Cavity Length with Curved Vane (Geometry 5) on Periodic Boundary (Run 5)

Bibliography

1. Anthenien, R., Mantz, R., Roquemore, W., and Sturgess, G., "Experimental Results for a Novel, High Swirl, Ultra Compact Combustor for Gas Turbine Engines," Air Force Research Laboratory, Wright-Patterson AFB, OH.
2. Armstrong, Jason M, "Effect of Equivalence Ratio on G-Loading on In-situ Measurements of Chemiluminescence in an Ultra Compact Combustor," M.S. thesis, Air Force Institute of Technology (AU), Wright-Patterson AFB, Ohio, March 2004.
3. ARP1533, "Procedure for the Calculation of Gaseous Emissions from Aircraft Turbine Engines" Society of Automotive Engineers, June 1996.
4. Blazek, J., *Computational Fluid Dynamics: Principles and Applications*, Elsevier Science, Ltd.,Kidlington, Oxford, UK, 2001.
5. Cohen, H., Rogers, GFC, and Saravanamuttoo, HIH, *Gas Turbine Theory*, T.J. Press, Padstow, Cornwall, 4th edition, 1996.
6. *FLUENT 6.1 User's Guide*, Fluent, Inc., Lebanon, NH, February 2003.
7. Glassman, Irvin, *Combustion*, Academic Press, 3rd Edition, 1996.
8. Hendricks, R.C., Shouse, D.T., Roquemore, W.M., and Burrus, D.L., "Experimental and Computational Study of Trapped Vortex Combustor Sector Rig with Tri-Pass Diffuser," NASA/TM–2004-212507, Jan 2004.
9. Hendricks, R.C., Ryder, R.C., Brankovic, A., Shouse, D.T., Roquemore, W.M., and Liu, N.-S., "Experimental and Computational Study of Trapped Vortex Combustor Sector Rig with Tri-Pass Diffuser," NASA/TM–2004-212507, Jan 2004.
10. Heywood, John B., *Internal Combustion Engine Fundamentals*, McGraw-Hill Book Company, 1988.
11. Hill, Philip G. and Peterson, Carl R., *Mechanics and Thermodynamics of Propulsion*, Addison-Wesley Publishing Company, Inc., 2nd Edition, 1992.
12. Hsu, K.-Y. and Goss, L.P., "Characteristics of a Trapped-Vortex Combustor," Journal of Propulsion and Power, Volume 14, No. 1, Jan-Feb 1998.
13. Incropera, Frank P. and DeWitt, David P., *Fundamentals of Heat and Mass Transfer*, John Wiley and Sons, Inc, 1990.
14. Lefebvre, Arthur H., *Gas Turbine Combustion*, Hemisphere Publishing Corporation, 1983.
15. Lewis, George D., "Centrifugal Force Effects on Combustion." Pratt and Whitney Aircraft, West Palm Beach, Florida.

16. Lewis, George D., "Swirling Flow Combustion–Fundamentals and Application," AIAA Paper No.73-1250, Pratt and Whitney Aircraft, West Palm Beach, Florida.

17. Little, B.H. and Whipkey, R.R., "Locked Vortex Afterbodies," Journal of Aircraft, Volume 16, No. 5, May 1979.

18. McMahon, P. J., *Aircraft Propulsion*, Harper and Row Publishers, Inc., 1971.

19. Mawid, M., Park, T., Thornburg, H., Sekar, B., and Zelina, J., "Numerical Analysis of Inter-Turbine Burner (ITB) Concepts for Improved Gas Turbine Engine Performance," AIAA 2005-1162.

20. Oates, Gordon C., *Aerothermodynamics of Gas Turbine and Rocket Propulsion*, American Institute of Aeronautics and Astronautics, Inc., Reston, Virginia, 3rd edition, 1997.

21. Oates, Gordon C., *Aircraft Propulsion Systems Technology and Design*, American Institute of Aeronautics and Astronautics, Inc., Washington, DC, 1989.

22. Quaale, Ryan, J. "Experimental Results for a High Swirl, Ultra Compact Combustor for Gas Turbine Engines," M.S. thesis, Air Force Institute of Technology (AU), Wright-Patterson AFB, Ohio, March 2003.

23. Roquemore, W.M., Shouse, D., Burrus, D., Johnson, A., Cooper, C., Duncan, B., Hsu, K.-Y., Katta, V.R., Sturgess, G.J., and Vihinen, I., "Trapped Vortex Combustor Concept for Gas Turbine Engines," AIAA 2001-0483, Jan 2001.

24. Sirignano, W.A. and Liu, F., "Performance Increases for Gas-Turbine Engines Through Combustions Inside the Turbine," Journal of Propulsion and Power, Volume 14, No. 6, Nov-Dec 1998.

25. Straub, D.L., Sidwell, T.G., Maloney, D.J., Casleton, K.H., and Richards, G.A., "Simulations of a Rich Quench Lean (RQL) Trapped Vortex Combustor," Presented at the AFRC International Symposium, Sept 2000.

26. Sturgess, G.J. and Hsu, K.-Y., "Combustion Characteristics of a Trapped Vortex Combustor," Innovative Scientific Solutions, Inc, Beavercreek, OH 45440.

27. Tannehill, J., Anderson D., and Pletcher, R., *Computational Fluid Mechanics and Heat Transfer*, Hemisphere Publishing Corporation., 2nd edition, 1997.

28. Yonezawa, Y., Toh, H., Goto, S., and Obata, M., "Development of the Jet-Swirl High Loading Combustor," AIAA-90-2451.

29. Zelina, J., Shouse, D.T., and Hancock, R.D., "Ultra-Compact Combustors for Advanced Gas Turbine Engines," ASME IGTI 2004-GT-53155.

30. Zelina, J., Sturgess, G.J., and Shouse, D.T., "The Behavior of an Ultra-Compact Combustor (UCC) Based on Centrifugally-Enhanced Turbulent Burning Rates," AIAA 2004-3541.

Vita

Captain Greenwood was born and raised in a small farming community in southeastern Idaho. After high school he went to Brigham Young University where he to work on a degree in Mechanical Engineering. After one year he left for two years to serve an LDS mission in Brazil. Upon returning he completed his degree while participating in the ROTC program. During his stay at BYU he got married and started a family. His first job took him to Hanscom AFB in Massachusetts where he worked for two and a half years as a project engineer at the Electronic Systems Center before coming to AFIT. His next assignment is to AFRL/PRTC. Captain Greenwood is married and has two daughters.

REPORT DOCUMENTATION PAGE

Form Approved
OMB No. 0704–0188

1. REPORT DATE *(DD–MM–YYYY)*	2. REPORT TYPE	3. DATES COVERED *(From — To)*
21–03–2005	Master's Thesis	Sep 2003 — Mar 2005

4. TITLE AND SUBTITLE

NUMERICAL ANALYSIS AND OPTIMIZATION OF THE ULTRA COMPACT COMBUSTOR

5a. CONTRACT NUMBER

5b. GRANT NUMBER

5c. PROGRAM ELEMENT NUMBER

6. AUTHOR(S)

Greenwood, Roger T., Capt, USAF

5d. PROJECT NUMBER

5e. TASK NUMBER

5f. WORK UNIT NUMBER

7. PERFORMING ORGANIZATION NAME(S) AND ADDRESS(ES)

Air Force Institute of Technology
Graduate School of Engineering and Management
2950 Hobson Way
WPAFB OH 45433-7765

8. PERFORMING ORGANIZATION REPORT NUMBER

AFIT/GAE/ENY/05-M10

9. SPONSORING / MONITORING AGENCY NAME(S) AND ADDRESS(ES)

AFOSR/NA
Dr. Julian Tishkoff
801 N. Randolph Street
Arlington VA 22203-7765

10. SPONSOR/MONITOR'S ACRONYM(S)

11. SPONSOR/MONITOR'S REPORT NUMBER(S)

12. DISTRIBUTION / AVAILABILITY STATEMENT

Approval for public release; distribution is unlimited.

13. SUPPLEMENTARY NOTES

14. ABSTRACT

In an effort to increase thrust per weight ratio and decrease pollutant emissions of aero-turbine jet engines, a circumferentially burning Ultra Compact Combustor (UCC) with a Cavity-in-a-Cavity design has been developed. A numerical analysis of this design has been conducted and compared with experimental results. The CFD model has been validated through a wide range of conditions and four alternative physical configurations of the UCC have been modeled. Emissions, combustor efficiencies, temperature and velocity profiles, and pressure drop values were used as comparison parameters. Numerical results indicate that increasing the outflow area will increase the pressure drop over the combustor and decrease the combustor efficiency. A significant decrease (250%) in the cavity circumferential velocity effectively decreased the fuel-air mixing in the cavity resulting in decreased combustion efficiencies. A decreased cavity length reduced combustor pressure drop significantly with only minimal increases in pollutant emissions. The addition of a curved vane to the decreased cavity length configuration further decreased the pressure drop.

15. SUBJECT TERMS

Combustion, Computational Fluid Dynamics, Emissions, Efficiency

16. SECURITY CLASSIFICATION OF:			17. LIMITATION OF ABSTRACT	18. NUMBER OF PAGES	19a. NAME OF RESPONSIBLE PERSON
a. REPORT	b. ABSTRACT	c. THIS PAGE			Ralph A. Anthenien, PhD, USAF (ENY)
U	U	U	UU	99	19b. TELEPHONE NUMBER *(include area code)* (937) 255–3636, ext 4643